JℳPAPERS

Blind disturbance separation and identification in a transitional boundary layer using minimal sensing

I. Gluzman[1],†, **J. Cohen**[1] **and Y. Oshman**[1]

[1]Faculty of Aerospace Engineering, Technion – Israel Institute of Technology, Haifa 3200003, Israel

A novel approach is presented for identifying disturbance sources in wall-bounded shear flows. The underlying approach models the flow state, as measured by sensors embedded in the flow, as a mixture of disturbance sources. The degenerate unmixing estimation technique is adopted as a blind source separation technique to recover the separate sources and their unknown mixing process. The efficiency of this approach stems from its ability to isolate any, *a priori* unknown, number of sources, using two sensors only. Furthermore, by adding a single additional sensor, the method is expanded to also determine the propagation velocity vector of each of the isolated sources, based on sensor readings from three sensors appropriately located in the flow field. Theoretical guidelines for locating the sensors are provided. The power of the method is demonstrated via computer simulations and wind-tunnel experiments. The numerical study considers disturbances comprising discrete Tollmien–Schlichting waves and wave packets. Linear stability theory is used to model source mixtures acquired by sensors placed in a Blasius boundary layer. The experimental study investigates the flow over a flat plate, with hot wires as sensors, and a loudspeaker and plasma actuators as source generators. Based on numerical and experimental demonstrations, it is believed that the new approach should prove useful in various applications, including active control of boundary layer transition from laminar to turbulent flow.

Key words: transition to turbulence, boundary layer control

† Currently a postdoctoral research associate at the Institute for Flow Physics and Control, Department of Aerospace and Mechanical Engineering, University of Notre Dame, Notre Dame, IN 46556, USA. Email address for correspondence: igluzman@nd.edu

1. Introduction

In flow control applications, model-based and rigorous design of controllers, using both experimental and simulation data, yields important insights into physical fluid systems for effective transition control. However, a major difficulty is to design feedback controllers for high-dimensional systems, such as those obtained by experiments or high-fidelity simulations, because of the prohibitive time and resource requirements. A more effective alternative is to rely on physical insights (Sturzebecher & Nitsche 2003; Opfer *et al.* 2004; Li & Gaster 2006; Greenblatt *et al.* 2008; Amitay, Tuna & Dell'Orso 2016; Vadarevu *et al.* 2019) to obtain approximations and simplifications for the governing equations, or to approximate the high-dimensional system using reduced-order models (Taylor & Glauser 2004; Rowley 2005; Schmid 2010; Brunton, Rowley & Williams 2013; Semeraro *et al.* 2013; Nicolò *et al.* 2015; Sipp & Schmid 2016; Taira *et al.* 2017) that retain those aspects of the flow that are relevant from a control perspective (Kim & Bewley 2007).

Following the new identification and isolation paradigm recently introduced by the authors (Gluzman, Oshman & Cohen 2020), in this paper we employ an alternative modelling approach that focuses on the physical disturbances that affect the flow field, such as those generated by sound or vorticity in the free stream, or by acoustic, mechanical or electrical actuators. These disturbances can modify the state of the field, i.e. its velocity, temperature or pressure, at a certain combination of position and time. The information we base on consists of flow field measurements that are acquired by sensors embedded in the field. We regard these measurements as consisting of mixtures of disturbance sources, where a disturbance source is defined as the signal recorded by the sensor due to the sole action of a particular physical disturbance. Each physical disturbance has its own uniquely generated time signature at a given sensor location. When several sources coexist, the resulting signal, measured by the sensor, is due to the combined effect of all the individual sources and their mutual interactions. Because the actual source-mixing process is usually unknown, it is a challenging task to discern the individual sources from the recorded signal. Source separation, as proposed in this work, is a process aiming at uniquely identifying the disturbance sources and the way they interact. Based on this process, one may relate the individual sources with distinct physical disturbance generators, and, thus, gain useful information about the disturbed flow field. In turn, this information can prove vital in, for example, the design of closed-loop strategies for the control of transitional boundary layers. Moreover, this new approach may provide new insights and perspectives on the way we study transitional flows.

Based on the information acquired by a limited number of sensors, we present a source separation method that can isolate and identify the sources mixed in each sensor measurement. The goal is to provide certain spatial and temporal behaviour characteristics of each source at the location of the sensors. These include the source time signature, propagation velocity and direction in the flow. We focus on disturbances in a boundary layer in which two types of disturbances are linearly superimposed: the first type is Tollmien–Schlichting (TS) waves and the second type is wave packets (WPs). The WP is in fact a superposition of many (theoretically infinite) TS waves. Introducing a disturbance to a boundary layer can cause the flow to transition from laminar to turbulent, through certain scenarios, depending on the disturbance characteristics (Schmid & Henningson 2001). In a quiet environment, the early stages of the transition process are governed by linear stability theory (LST), which assumes a linear superposition of the disturbance mixture. In these cases, LST can predict the downstream evolution of the combined disturbances.

Our novel approach of identifying the sources from measured mixtures in shear flow is based on adapting a blind source separation (BSS) technique. Known to be very

useful in image processing (Vigario & Oja 2008; Silva *et al.* 2020), mechanical systems (Antoni 2005; Serviere & Fabry 2005; Zhang *et al.* 2017) and acoustical applications (Sawada, Araki & Makino 2010; Yoshioka *et al.* 2010; Nogueira & Petraglia 2015), BSS methods were originally developed for solving the problem of separating linear convolutive mixtures in acoustic applications, known as the cocktail party problem. In that problem, the goal is to identify the sources of speech pressure waves generated by simultaneously active and independent speakers in the same room (Cherry 1953; Haykin & Chen 2005). Similar applications can be found in brain imaging data for recovering the original components of brain activity from recorded mixed data, acquired by an electroencephalogram. Source separation has also been applied to astronomical data or satellite images, finding hidden factors in financial data and reducing noise in natural images. For more applications, see Haykin & Chen (2005) and Pedersen *et al.* (2007) and references therein. Recent developments in BSS methods are based on sparsity-inducing techniques, such as the sparse component extraction algorithm that was proposed by Gao *et al.* (2018) for diagnostic imaging systems, and unsupervised data decomposition techniques, such as the non-negative matrix factorization methodology (Ozerov & Fevotte 2010), and their extensions to three-dimensional non-negative tensor factorization (Cichocki, Zdunek & Amari 2007). A broad survey of models and efficient algorithms of non-negative matrix factorization and non-negative tensor factorization for BSS is provided in Cichocki *et al.* (2009).

In a recent study by the authors (Gluzman *et al.* 2020), the celebrated independent component analysis (ICA) (Hyvärinen & Oja 2000) technique was used as a BSS method for the detection and isolation of TS waves in subcritical transitional shear flows based on high-order statistics of the measured signals. The application of the method to measured mixtures from numerical and experimental data has been studied, demonstrating the viability of the method. The efficacy of the method depends on compliance with physics-based sensor placement design rules that resolve the inherent incompatibility between the ICA instantaneous (delay-less) mixture model and the physical mixing process in the considered shear flows. These rules require prior, physics-based, information on the number of sources and the wavelengths of the TS disturbances present in the flow. In turn, this information dictates the required number of sensors, and their relative placement with respect to each other. It is the goal of the present paper to relax the aforementioned structural requirements of the ICA-based method (Hyvärinen & Oja 2000), thereby extending and fully exploiting the scope of BSS methods to discover and learn about the mixing process of the flow only from available sensor measurements, not requiring any prior information on the sources.

The contributions of this paper are twofold. The first is a method for separating individual disturbance sources that are present in source mixtures measured in a shear boundary layer, using the degenerate unmixing estimation technique (DUET), introduced in Yilmaz & Rickard (2004) and Rickard (2007). Unlike ICA-based BSS techniques, which rely on non-Gaussianity criteria to separate sources, DUET relies on the assumption that the signals are sparse in the time–frequency domain, and was shown to sustain robust performance in noisy environments (Kim *et al.* 2006; Zhen *et al.* 2017). Characterized by its ability to handle degenerate mixtures, that is, mixtures characterized by fewer sensors than sources, the DUET BSS method is used in this paper to isolate any number of sources using two sensors only, which renders it very efficient relative to other BSS techniques. Exploiting the DUET-based BSS method, the second contribution is a method for determining the propagation velocity vector of each of the identified sources, from measurements acquired by as few as three sensors appropriately placed in the flow field.

These two contributions are demonstrated both numerically and experimentally. The numerical study employs LST to model the measured source mixtures acquired by sensors placed in a Blasius boundary layer (BBL). The disturbances that are modelled to be active in the boundary layer are three-dimensional TS waves and WPs, which may propagate downstream in parallel or at a certain angle to the free-stream direction. Carried out in a wind tunnel, the experimental study considers the flow over a flat plate, with hot wires as sensors and a loudspeaker and plasma actuators as source generators.

The remainder of this paper is organized as follows. In § 2 we present the DUET-based BSS method for separating the disturbance sources present in source mixtures acquired by sensors placed in the flow field. Using this DUET-based method, we show in § 3 how to estimate the propagation velocity of disturbances via three sensors appropriately placed in the flow field. Sections 4 and 5 provide numerical and experimental proofs of concept, respectively, for the new methods. Finally, conclusions are drawn in § 6.

2. Blind source separation via DUET

For completeness, we review in this section the main assumptions and procedures for implementing DUET. For more details, the reader is referred to Yilmaz & Rickard (2004) and Rickard (2007).

2.1. *Overview of DUET*

For blindly separating an arbitrary number of sources with only two provided source mixtures, DUET relies on the following assumptions:

(i) *Anechoic mixing model.* Originally developed for signal processing in acoustical applications, DUET assumes an anechoic mixing model. Accordingly, the signals of N_s mixed sources that are measured by two sensors can be described as

$$x_1(t) = \sum_{j=1}^{N_s} s_j(t), \tag{2.1a}$$

$$x_2(t) = \sum_{j=1}^{N_s} a_j s_j(t - \delta_j), \tag{2.1b}$$

where $x_1(t)$ and $x_2(t)$ are the measurements of sensor 1 and sensor 2, respectively. Here, δ_j is the time it takes source s_j to travel from the location of sensor 1 to the location of sensor 2 and a_j is the relative attenuation (amplitude growth or decay) of source s_j as measured in sensor 2 relative to how it is measured in sensor 1.

(ii) *Windowed-disjoint orthogonality (WDO) of sources.* A basic assumption is that the signals are sufficiently sparse so that, at most, one source is dominant at each time–frequency point. In other words, DUET assumes that the sources are disjoint in the time–frequency domain. Mathematically stated, DUET assumes WDO of sources, where the following definition is used: two sources $s_j(t)$ and $s_k(t)$ are windowed-disjoint orthogonal if

$$\hat{s}_j(\tau, \omega)\hat{s}_k(\tau, \omega) = 0, \quad \forall \tau, \omega \text{ and } \forall j \neq k. \tag{2.2}$$

In (2.2), $\hat{s}_j(\tau, \omega)$ is the short-time Fourier transform, or windowed transform, of $s_j(t)$, defined as

$$\hat{s}_j(\tau, \omega) = \mathcal{F}^W[s_j](\tau, \omega) \triangleq \frac{1}{2\pi} \int_{-\infty}^{\infty} W(t - \tau) s_j(t) \, \mathrm{e}^{-\mathrm{i}\omega t} \, \mathrm{d}t, \qquad (2.3)$$

where $W(t - \tau)$ is the Hann window function centred at τ, $\omega = 2\pi f$ where f is the frequency (having the units of τ^{-1}) and $\mathrm{i} = \sqrt{-1}$.

(iii) *Local stationarity.* The DUET algorithm assumes that, for a given sensor spatial separation (see next assumption), source propagation speed and selected time window, the sources comprising the measured mixtures are locally stationary, i.e. they satisfy

$$\mathcal{F}^W[s_j(t - \delta_j)](\tau, \omega) = \mathrm{e}^{-\mathrm{i}\omega\delta_j} \mathcal{F}^W[s_j(t)](\tau, \omega), \quad \forall \delta_j \text{ such that } |\delta_j| < \Delta, \quad (2.4)$$

where Δ is the maximum possible time difference in the mixing model. The time difference Δ can be obtained by dividing the distance between the sensors by the slowest source propagation speed.

(iv) *Sensor spatial separation.* DUET estimates the delay δ_j from the $\mathrm{e}^{-\mathrm{i}\omega\delta_j}$ term (this is shown next). There are infinitely many possible estimates of δ_j based on that term, all satisfying $\delta_j = \delta + 2\pi k$ for $k \in \mathbb{Z}$ (this integer ambiguity is also called the wrap-around problem). To circumvent this problem without having to solve for the unknown integer delays, it is assumed that the distance between sensors, Δr, is sufficiently small, so as to guarantee a unique solution. We thus require

$$|\omega\delta_j| < \pi, \quad \forall \omega \text{ and } \forall j, \qquad (2.5)$$

which leads to the following condition on the distance between sensors:

$$\Delta r < \frac{\pi U}{\omega_m}, \qquad (2.6)$$

where ω_m is the maximum frequency present in the mixture and U is the speed of the slowest disturbance source in the mixture. This constraint can be removed using various DUET extensions, as proposed by Rickard (2007) and Wang, Yılmaz & Zhou (2013).

(v) *Signal signature diversity.* If two sources have identical spatial signatures, that is, identical relative attenuations and relative delays (mixing parameters), then they can be combined into one source without changing the model, rendering them inseparable by DUET. We thus assume that

$$(a_j \neq a_k) \text{ or } (\delta_j \neq \delta_k), \quad \forall j \neq k. \qquad (2.7)$$

Assumptions (i)–(iii) yield

$$\begin{bmatrix} \hat{x}_1(\tau, \omega) \\ \hat{x}_2(\tau, \omega) \end{bmatrix} = \begin{bmatrix} 1 \\ a_j \, \mathrm{e}^{-\mathrm{i}\omega\delta_j} \end{bmatrix} \hat{s}_j(\tau, \omega), \quad \forall(\tau, \omega). \qquad (2.8)$$

The WDO assumption means that only a single source s_j can be active at a certain point (τ, ω) in the time–frequency domain. In the interest of practicality, we relax this assumption and require, alternatively, that if several sources are active at the same time–frequency point, then one of them is dominant, in the sense that it can be regarded as

the single active source at that time–frequency point. Dividing $\hat{x}_2$ by $\hat{x}_1$ in (2.8), we thus obtain

$$\frac{\hat{x}_2(\tau, \omega)}{\hat{x}_1(\tau, \omega)} \approx a_j \, \mathrm{e}^{-\mathrm{i}\omega\delta_j}, \quad \forall(\tau, \omega) \in \Omega_j, \tag{2.9}$$

where Ω_j is defined as the set of time–frequency pairs (τ, ω) for which the sources are sufficiently sparse so that, at most, one of them is dominant at each time–frequency combination, i.e.

$$\Omega_j \triangleq \{(\tau, \omega) \mid |\hat{s}_j(\tau, \omega)| \gg |\hat{s}_k(\tau, \omega)| \, \forall k \neq j\}. \tag{2.10}$$

The important result of (2.9) is that the ratio of the short-time Fourier transformed signals, $\hat{x}_2(\tau, \omega)/\hat{x}_1(\tau, \omega)$, does not depend on the signals themselves, but on their mixing parameters a_j and δ_j only. In DUET, the sources s_j are identified via estimation of a_j and δ_j. This is done by local estimation of the mixing parameters, $\tilde{a}$ and $\tilde{\delta}$, for each time–frequency pair (τ, ω) and a combination of the set of local mixing-parameter estimates into N_s pairings corresponding to the true mixing-parameter pairings. From (2.9), for each time–frequency point (τ, ω), we obtain local estimates of the relative delay, $\tilde{\delta}(\tau, \omega)$, and the relative attenuation, $\tilde{a}(\tau, \omega)$, as

$$\tilde{\delta}(\tau, \omega) \approx -\frac{1}{\omega} \arg\left(\frac{\hat{x}_2(\tau, \omega)}{\hat{x}_1(\tau, \omega)}\right), \tag{2.11}$$

$$\tilde{a}(\tau, \omega) \approx \left|\frac{\hat{x}_2(\tau, \omega)}{\hat{x}_1(\tau, \omega)}\right|. \tag{2.12}$$

For convenience, the relative attenuation $\tilde{a}$ is replaced by the symmetric relative attenuation $\tilde{\alpha}$:

$$\tilde{\alpha} \triangleq \tilde{a} - \frac{1}{\tilde{a}}. \tag{2.13}$$

According to (2.13), $\tilde{\alpha}$ changes sign when sensors are swapped. Under assumptions (iv) and (v), the local symmetric relative attenuation and delay estimates, $\tilde{\alpha}(\tau, \omega)$ and $\tilde{\delta}(\tau, \omega)$, respectively, should be related to the actual $\alpha_j(\tau, \omega)$ and $\delta_j(\tau, \omega)$ of each source s_j. In other words, the union of the $(\tilde{\alpha}(\tau, \omega), \tilde{\delta}(\tau, \omega))$ pairs, taken over all (τ, ω) combinations, is the set of N_s (α_j, δ_j) pairs:

$$\{(\alpha_j, \delta_j) \mid j = 1, \ldots, N_s\} = \bigcup_{(\tau, \omega)} \{\tilde{\alpha}(\tau, \omega), \tilde{\delta}(\tau, \omega)\}. \tag{2.14}$$

For source separation, binary masks are generated by

$$M_j(\tau, \omega) = \begin{cases} 1 & (\tilde{a}(\tau, \omega), \tilde{\delta}(\tau, \omega)) = (a_j, \delta_j), \\ 0 & \text{otherwise.} \end{cases} \tag{2.15}$$

Finally, the separation of sources is obtained by multiplying each mask with one of the mixtures.

2.2. *Implementation of DUET*

The implementation of DUET is based on transforming (2.14) and (2.15) to operational relations. In Yilmaz & Rickard (2004), it was found that in the approximate WDO case,

the instantaneous DUET estimates $\tilde{a}(\tau, \omega)$, $\tilde{\delta}(\tau, \omega)$ (equations (2.11) and (2.13)) are not identically related to the actual mixing parameters (α_j, δ_j) of the original N_s sources, but they cluster around them. Therefore, the realization of (2.14) is obtained by construction of a two-dimensional weighted histogram for determining these clusters. The histogram domain, $I(\alpha, \delta)$, is defined over $\tilde{a}(\tau, \omega)$, $\tilde{\delta}(\tau, \omega)$ as follows:

$$I(\alpha, \delta) \triangleq \{(\tau, \omega) \mid |\tilde{\alpha}(\tau, \omega) - \alpha| < \Delta_\alpha, |\tilde{\delta}(\tau, \omega) - \delta| < \Delta_\delta\}, \tag{2.16}$$

where Δ_α and Δ_δ are smoothing resolution widths. Using the $\tilde{a}(\tau, \omega)$, $\tilde{\delta}(\tau, \omega)$ pairs to indicate the indices of the histogram and using $|\hat{x}_1(\tau, \omega)\hat{x}_2(\tau, \omega)|^p \omega^q$ for the weight, a two-dimensional weighted histogram is constructed:

$$H(\alpha, \delta) \triangleq \iint_{(\tau, \omega) \in I(\alpha, \delta)} |\hat{x}_1(\tau, \omega)\hat{x}_2(\tau, \omega)|^p \omega^q \, d\tau \, d\omega. \tag{2.17}$$

Here, p and q are variables of a weighted average, which, by default, are set to $p = 1$, $q = 0$ (Yilmaz & Rickard 2004). If assumptions (i)–(v) hold, (2.17) takes the form

$$H(\alpha, \delta) = \begin{cases} \iint_{(\tau, \omega) \in I(\alpha, \delta)} |\hat{s}_j(\tau, \omega)|^{2p} \omega^q \, d\tau \, d\omega & |\alpha_j - \alpha| < \Delta_\alpha, \ |\delta_j - \delta| < \Delta_\delta, \\ 0 & \text{otherwise.} \end{cases} \tag{2.18}$$

The weighted histogram separates and clusters the parameter estimates of each source. The number of peaks reveals the number of sources, and the peak locations reveal the associated source's anechoic mixing parameters, which are denoted by $(\tilde{\alpha}_j, \tilde{\delta}_j)$. Then, the relative estimated attenuation $\tilde{a}_j$ is retrieved from the estimated symmetric attenuation $\tilde{\alpha}_j$ by

$$\tilde{a}_j = \frac{\tilde{\alpha}_j + \sqrt{\tilde{\alpha}_j^2 + 4}}{2}. \tag{2.19}$$

Next, N_s estimated pairs $(\tilde{\alpha}_j, \tilde{\delta}_j)$ should be related back to each time–frequency point (τ, ω) which is closest to the local parameter estimates $(\tilde{\alpha}(\tau, \omega), \tilde{\delta}(\tau, \omega))$. Following Yilmaz & Rickard (2004), a maximum-likelihood association rule (estimator) for the jth source is obtained as

$$J(\tau, \omega) \triangleq \arg\min_j \frac{|\tilde{a}_j \, e^{-i\tilde{\delta}_j \omega} \hat{x}_1(\tau, \omega) - \hat{x}_2(\tau, \omega)|^2}{1 + \tilde{a}_j^2}. \tag{2.20}$$

These obtained estimators are used to obtain N_s binary masks, as follows:

$$\tilde{M}_j(\tau, \omega) = \begin{cases} 1 & J(\tau, \omega) = j, \\ 0 & \text{otherwise,} \end{cases} \tag{2.21}$$

and the maximum-likelihood source estimates are obtained, as proposed in Yilmaz & Rickard (2004), based on maximum-likelihood estimates of $(\tilde{\alpha}_j, \tilde{\delta}_j)$, as

$$\hat{s}_j(\tau, \omega) = \tilde{M}_j(\tau, \omega) \frac{\hat{x}_1(\tau, \omega) + \tilde{a}_j \, e^{i\tilde{\delta}_j \omega} \hat{x}_2(\tau, \omega)}{1 + \tilde{a}_j^2}. \tag{2.22}$$

In summary, implementing DUET consists of the following main steps (we assume that two mixtures are acquired):

(i) Construct time–frequency representations of both mixtures: $\hat{x}_1(\tau, \omega)$, $\hat{x}_2(\tau, \omega)$.

(ii) Extract local mixing-parameter estimates: $\tilde{a}(\tau, \omega)$, $\tilde{\delta}(\tau, \omega)$.

(iii) Out of the set of local mixing-parameter estimates, form N_s parameter pairings, optimally corresponding to the true mixing-parameter pairings: $(\tilde{a}_1, \tilde{\delta}_1), \ldots, (\tilde{a}_{N_s}, \tilde{\delta}_{N_s})$.

(iv) For each determined mixing-parameter pair, generate a binary mask corresponding to the time–frequency points that yield that particular mixing-parameter pair: $M_1(\tau, \omega), \ldots, M_{N_s}(\tau, \omega)$.

(v) Isolate (demix) the sources by applying each mask to both mixtures. This yields: $\hat{s}_1(\tau, \omega), \ldots, \hat{s}_{N_s}(\tau, \omega)$.

(vi) Finally, transform each demixed time–frequency representation to the time domain, yielding the isolated sources $s_1(t), \ldots, s_{N_s}(t)$.

In the following we extend the DUET-based method to also determine the propagation velocity vector of each of the identified sources.

3. Estimation of disturbance propagation velocity via DUET

The method proposed herein for determining the source propagation velocity (direction and speed) is based on sampling the flow in several different locations and then using the DUET method on these samples. Regarding a particular sensor, each source is characterized by two parameters: (1) the direction from which the source is arriving and (2) its distance relative to the sensor. Let δ_{ikj} denote the relative delay of arrival of a specific source s_j, between two sensors, x_i and x_k. We define δ_{ikj} to be positive if the source first arrives at sensor x_i and then at x_k, and negative vice versa. Thus, the sign of δ_{ijk} (by itself) provides a partial indication of the source direction. The observation underlying the method presented in this section is that the DUET algorithm can provide an estimate of δ_{ikj}. This estimate can, in turn, be used to estimate the propagation direction of the source.

Assuming three sensors, the geometrical model of the source propagation direction determination problem is schematically depicted in figure 1. In addition to the assumptions used to blindly separate the sources using DUET, we add the following three assumptions:

(i) Each source is assumed to possess a uniform planar wave front, i.e. the source wave front's curvature is neglected.

(ii) The dispersive nature of a WP source is neglected, so that its group velocity is taken to represent the velocity of the source.

(iii) The sensors are assumed to be omni-directional, i.e. capable of measuring sources arriving from any direction.

These assumptions generally hold for disturbances in transitional flows. In particular, the first assumption is valid if the source is formed sufficiently far away from the sensors, which means that, compared with the distances between the sensors, the distance between the point of creation of the source and the sensors is large. The second assumption is valid for WP sources if the sensors are placed close to each other (which can be regarded as a design constraint). Being somewhat more restrictive, the third assumption does not strictly hold for a single hot-wire sensor, measuring the fluid velocity component perpendicular to the hot wire. Nevertheless, as is demonstrated in what follows, even flow components arriving at oblique angles to the wire can still be captured, albeit at an attenuated level.
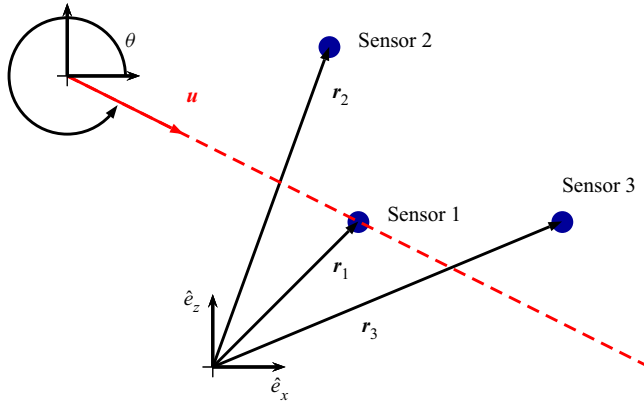
927 A4-8

Figure 1. Measurement geometry of a source with velocity $\boldsymbol{u}$. Three sensors are used.

3.1. *Method derivation*

Our approach for source propagation direction determination derives from that of Oshman & Markley (1999), where a global positioning system (GPS) antenna array is used for spacecraft attitude estimation, based on measuring the phase difference between GPS signals acquired by the antenna array.

Consider a source s that propagates in the x–z plane with velocity

$$\boldsymbol{u} = u\hat{\boldsymbol{u}}, \tag{3.1}$$

where the source speed is $u = |\boldsymbol{u}|$ and $\hat{\boldsymbol{u}}$ is a unit directional vector. Our goal is to determine this velocity (both direction and magnitude) for each source from source mixtures measured by N sensors.

We position N sensors in the flow located at $\boldsymbol{r}_{x_i}$, $i = 1, \ldots, N$, in the x–z plane ($N = 3$ in figure 1). Analogously to the GPS antenna array of Oshman & Markley (1999), we denote sensor 1 as the master sensor and, accordingly, sensors $2, \ldots, N$ as the slave sensors. This sensor array configuration defines $N - 1$ baseline vectors, $\boldsymbol{r}_{x_i} - \boldsymbol{r}_{x_1}$, $i = 2, \ldots, N$. As in GPS attitude determination problems, here, too, a minimum of two baselines are required, corresponding to a minimal configuration of three sensors.

The source s that travels from the master sensor (sensor 1) to slave sensor i, $i = 2, \ldots, N$, covers the distance

$$(\boldsymbol{r}_{x_i} - \boldsymbol{r}_{x_1})^{\mathrm{T}}\hat{\boldsymbol{u}} = \delta_i u, \quad i = 2, \ldots, N, \ N \geq 3, \tag{3.2}$$

where we have used a shorthand notation for the delay δ_i, and $\delta_i > 0$ ($\delta_i < 0$ with the same magnitude if the source travels in the opposite direction). We now use the normalized baseline vectors to define the rows of the matrix $\boldsymbol{W} \in \mathbb{R}^{N-1,2}$:

$$\boldsymbol{W} \triangleq \begin{bmatrix} \delta_2^{-1}(\boldsymbol{r}_{x_2} - \boldsymbol{r}_{x_1})^{\mathrm{T}} \\ \delta_3^{-1}(\boldsymbol{r}_{x_3} - \boldsymbol{r}_{x_1})^{\mathrm{T}} \\ \vdots \\ \delta_N^{-1}(\boldsymbol{r}_{x_N} - \boldsymbol{r}_{x_1})^{\mathrm{T}} \end{bmatrix}. \tag{3.3}$$

Then, (3.2) can be rewritten as

$$u^{-1}\boldsymbol{W}\hat{\boldsymbol{u}} = \boldsymbol{1}, \tag{3.4}$$

where all entries of the vector $\mathbf{1} \in \mathbb{R}^{N-1}$ are ones. Equation (3.4) is a system of $N-1$ linear equations for the speed u and the independent entry of the direction vector $\hat{\boldsymbol{u}}$. For $N = 3$, this system has a unique solution if the columns of $\boldsymbol{W}$ are independent, which corresponds to a three-sensor configuration having two non-collinear baselines. For $N > 3$, the system becomes overdetermined, calling for a least squares solution, a minimum-norm version of which is provided by the Moore–Penrose pseudoinverse of $\boldsymbol{W}$, which can be robustly computed using the singular value decomposition.

3.2. *Sensor configuration design*

Relative to some given disturbance direction, the configuration of the N sensors determines the numerical properties of the linear system (3.4), which, in turn, determine the quality of the solution for the disturbance propagation velocity. We use the condition number of the coefficient matrix, denoted as $\kappa(\boldsymbol{W})$, which is the ratio between the largest and smallest singular values of $\boldsymbol{W}$, as a measure of the quality of the solution. A small condition number, i.e. a condition number close to one, means that the system is well-conditioned, and a high-quality solution may be expected. On the other hand, a large condition number is associated with an ill-conditioned system, leading to a solution of poor quality, due to system sensitivity to small input errors.

Evaluating the condition number as a function of the sensor configuration and disturbance direction can naturally assist in the following two sensor design tasks:

(i) Given a certain sensor configuration, $\kappa(\boldsymbol{W})$ can be used to find the unobservable directions; that is, the disturbance directions that cannot be identified using the given configuration.

(ii) Given the disturbance direction, $\kappa(\boldsymbol{W})$ can be used to design the best sensor configuration for the task of disturbance velocity estimation.

In what follows, we demonstrate the above two tasks via illustrative examples.

3.2.1. *Unobservable directions for a given sensor configuration*

In this subsection, we demonstrate how the $\kappa(\boldsymbol{W})$ measure may assist in finding the unobservable directions associated with a given three-sensor configuration. The disturbance speed is set to be $|\boldsymbol{u}| = 1 \text{ m s}^{-1}$ and the velocity direction, represented by the angle θ with respect to $\hat{\boldsymbol{e}}_x$ as displayed in figure 1, is varied between $0°$ and $360°$ at 4001 points uniformly spread in this range.

In the top three panels of figure 2, we illustrate three different three-sensor configurations, all consisting of a master sensor 1 (marked by the symbol $\times$) and two slave sensors 2 and 3 (marked as small circle and square, respectively). The two baselines are illustrated by arrows, pointing from the master sensor to the slave sensors. The bottom three panels of figure 2 present the value of the $\kappa(\boldsymbol{W})$ measure on polar coordinates as a function of θ, the disturbance arrival direction. The radial distance from the origin stands for the value of $\kappa(\boldsymbol{W})$, and the two circles in each of these plots correspond to the values of $\kappa(\boldsymbol{W}) = 2.5$ (inner dotted circle) and $\kappa(\boldsymbol{W}) = 5$ (outer circle). Disturbance arrival angles corresponding to $\kappa(\boldsymbol{W}) \geq 50$ are marked in these plots by red arcs on the outer circle. The ill-conditioning threshold value of 50 is arbitrarily chosen; clearly, disturbance sources arriving from directions corresponding to angles within the red arcs may not be determined correctly. As may be expected, figure 2(*c*) reveals that when the two baselines are collinear, the entire polar domain is unobservable.
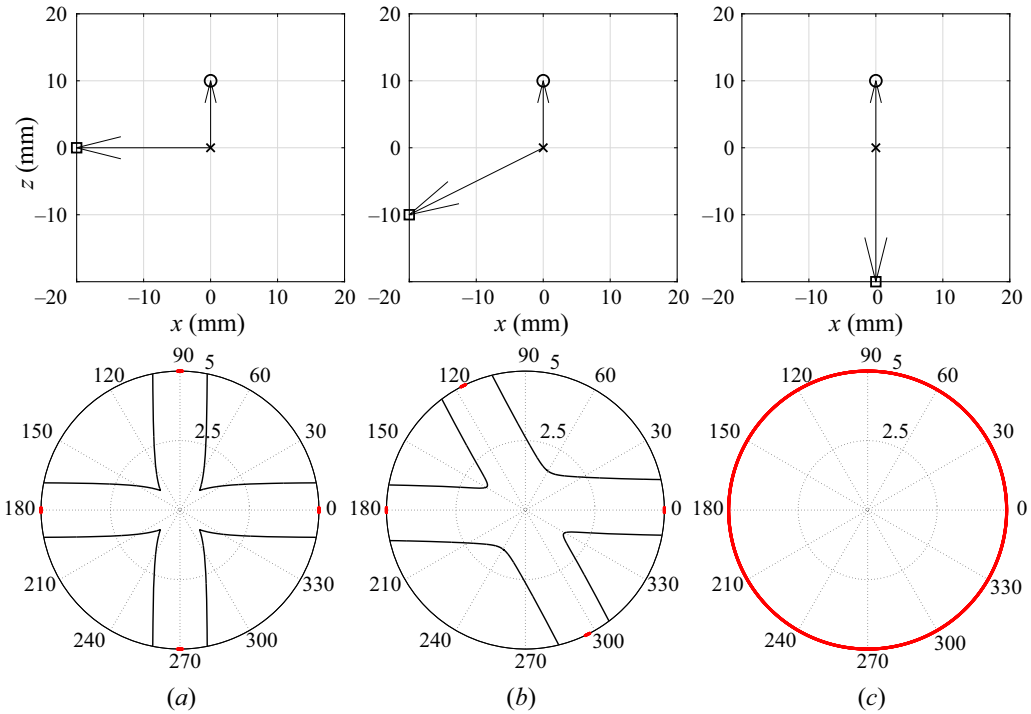
Figure 2. Unobservable directions for (*a–c*) three sensor configurations. Top panels: sensor configurations. Master sensor marked by ×, slave sensors marked by circle and square symbols, baselines denoted by arrows. Bottom panels: polar plots of $\kappa(\boldsymbol{W})$ versus disturbance arrival direction. Angles associated with $\kappa(\boldsymbol{W}) \geq 50$ are shown via red arcs on the outer circles (that correspond to $\kappa(\boldsymbol{W}) = 5$).

3.2.2. *Best sensor configuration for a given disturbance direction*

We next demonstrate how the $\kappa(\boldsymbol{W})$ measure is used to design the optimal sensor configuration for a given disturbance direction. The disturbance speed is set to $|\boldsymbol{u}_j| = 1 \text{ m s}^{-1}$ and the disturbance arrival angle varies between (a) $\theta = -90°$, (b) $\theta = -60°$, (c) $\theta = -20°$ and (d) $\theta = 0°$. Two sensors are fixed, whereas the location of the third sensor varies within the range $x, z \in [-50, 50]$ mm, with 1 mm step in each direction. Figure 3 displays the value of $\kappa(\boldsymbol{W})$ for all possible locations of the third sensor in the *x–z* plane. Regions of the *x–z* plane associated with high values of $\kappa(\boldsymbol{W})$ should be avoided. In figure 3(*d*), the first slave sensor is located such that its baseline is perpendicular to the disturbance velocity vector, which results in $\delta_{12} = 0$. Therefore, $\kappa(\boldsymbol{W}) \to \infty$ for any location of the second slave sensor, rendering the determination of the velocity vector in this configuration impossible. In general, figure 3(*d*) demonstrates that the problem becomes unobservable if the sensors are configured such that either (1) at least one baseline is perpendicular to the disturbance velocity vector or (2) the baselines are collinear.

4. Numerical study

To study the performance of the DUET method and demonstrate computationally our method of estimating disturbance propagation velocity, we utilize LST to model the evolution of source mixtures in a BBL. We further use LST predictions as guidelines for designing the experimental set-up and determining the operational conditions of the experiments.
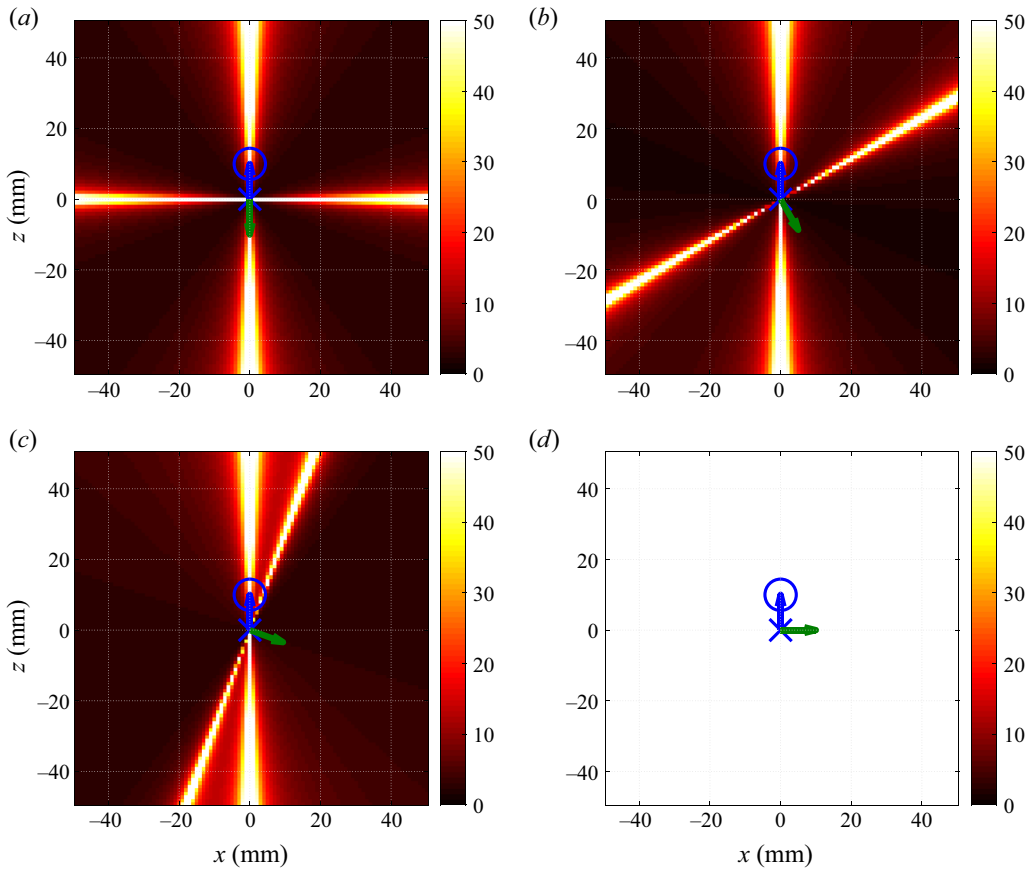
Figure 3. The $\kappa(\boldsymbol{W})$ measure as a function of the location of the third sensor, when the first two sensors (marked by the $\times$ and circle symbols) are fixed, for four different disturbance arrival angles: (a) $\theta = -90°$, (b) $\theta = -60°$, (c) $\theta = -20°$ and (d) $\theta = 0°$. The disturbance velocity vector is represented by the green arrow and the baseline vector between the first two sensors is denoted by the blue arrow.

4.1. *Generating disturbance source model via LST*

We consider incompressible wall-bounded parallel shear flow with streamwise direction (x), wall-normal direction (y) and spanwise direction (z). We decompose the total velocity field into a base flow of the form $\boldsymbol{U} = [U(y)\ 0\ 0]^{\mathrm{T}}$ and perturbed ($\boldsymbol{u}^{(1)}, p^{(1)}$) states about the base flow. All quantities are non-dimensionalized by the free-stream velocity, U_∞, and the boundary layer displacement thickness, δ_d, at a given streamwise position. This renders the Reynolds number $Re = U_\infty \delta_d / \nu$ as the governing parameter, where ν is the kinematic viscosity of the flow. The linearized Navier–Stokes equations are obtained by subtracting the equations for the base state from those corresponding to the total state, and dropping the nonlinear terms.

We analyse the stability of the mean flow with respect to wavelike velocity and pressure perturbations, also known as normal modes, for which

$$q^{(1)} = \hat{q}(y)\, \mathrm{e}^{\mathrm{i}(\alpha x + \beta z - \omega t)}, \tag{4.1}$$

where $q^{(1)} = [u^{(1)}\ v^{(1)}\ w^{(1)}\ p^{(1)}]^{\mathrm{T}}$, and $\hat{q}(y) = [\hat{u}(y)\ \hat{v}(y)\ \hat{w}(y)\ \hat{p}(y)]^{\mathrm{T}}$ is the corresponding complex eigenvector. We consider the spatial case in which α is a complex
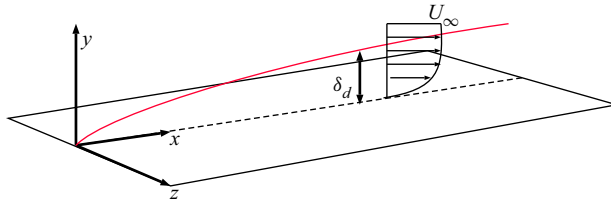
927 A4-12

Figure 4. Flow over a flat plate.

eigenvalue; $\alpha_r \triangleq \mathrm{Re}(\alpha)$ and β are the disturbance streamwise and spanwise wavenumbers, respectively; $\alpha_{im} \triangleq \mathrm{Im}(\alpha)$ is the disturbance streamwise decay/growth rate for positive and negative values, respectively; and ω is the dimensionless disturbance frequency. Substituting (4.1) into the linearized Navier–Stokes equations (which is equivalent to taking the Fourier transform) results in the following dispersion relation:

$$\mathbb{D}(\alpha, \beta, \omega) = 0. \tag{4.2}$$

This constitutes an eigenvalue problem for the complex eigenvalue α and its corresponding eigenfunction $\hat{q}$, for the given spanwise wavenumber β, the real frequency ω, the Reynolds number Re and the base flow velocity profile $U(y)$.

Following the primitive variable formulation in Schmid & Henningson (2001, p. 290), the dispersion relation (4.2) for the spatial case translates to the following system of equations:

$$\begin{bmatrix} 0 & -D & -\mathrm{i}\beta & 0 & 0 & 0 \\ 0 & 0 & 0 & 0 & 1 & 0 \\ 0 & 0 & 0 & 0 & 0 & 1 \\ C & T & \mathrm{i}U\beta & 0 & -D/Re & -\mathrm{i}\beta/Re \\ 0 & -ReC & 0 & ReD & ReU & 0 \\ 0 & 0 & -ReC & \mathrm{i}\beta Re & 0 & ReU \end{bmatrix} \begin{bmatrix} \hat{u} \\ \hat{v} \\ \hat{w} \\ \hat{p} \\ \hat{v}_x \\ \hat{w}_x \end{bmatrix} = \mathrm{i}\alpha \begin{bmatrix} \hat{u} \\ \hat{v} \\ \hat{w} \\ \hat{p} \\ \hat{v}_x \\ \hat{w}_x \end{bmatrix}, \tag{4.3}$$

with homogeneous boundary conditions. For example, in BBL, $\hat{u} = \hat{v} = \hat{w} = \hat{v}_x = \hat{w}_x = 0$ at $y = 0$ and $y \to \infty$ (see figure 4). Here C and T denote the linear operators $C \triangleq \mathrm{i}\omega + (D^2 - \beta^2)/Re$ and $T \triangleq UD - U_y$. Both subscript $(\cdot)_y$ and operator D denote the first derivative with respect to y, whereas $(\cdot)_x$ denotes the first derivative with respect to x.

Thus, we have a boundary value problem for the above system, which we solve numerically with the aid of Matlab, utilizing spectral methods (Trefethen 2000) with 150 grid points. The results of the numerical dispersion relation solution are validated against reported results in the literature for the BBL (Jordinson 1970; Schmid & Henningson 2001; Boiko *et al.* 2011). We search for the most unstable TS wave, where its eigenmode is obtained from (4.3), and its amplitude profile is represented by the corresponding $|\hat{q}(y)|$.

In addition to TS waves we also consider WP sources. A single WP disturbance may be generated by a short pulse actuation of the boundary layer at a specific location. The short pulse generates a localized disturbance that may be regarded as a linear superposition of many TS waves associated with a wide range of frequencies that may grow or decay downstream in the boundary layer. We focus on the long-time instability characteristics of the WP, far away from the pulse actuation location, after the WP transient behaviour

has decayed. Each of the WP modes travels with its own phase velocity, given by

$$c_r = [c_x \quad c_z]^T = \boldsymbol{k}\frac{\omega}{|\boldsymbol{k}|^2}, \tag{4.4}$$

but all modes share the same group velocity:

$$c_g = \nabla_k \omega. \tag{4.5}$$

In (4.5), $\nabla_k = [\partial/\partial\alpha \quad \partial/\partial\beta]^T$ and $\boldsymbol{k}$ is a real wavenumber vector, defined as

$$\boldsymbol{k} \triangleq [\text{Re}\{\alpha\} \quad \beta]^T, \tag{4.6}$$

i.e. $c_x = \text{Re}\{\alpha\}\omega/|\boldsymbol{k}|^2$ and $c_z = \beta\omega/|\boldsymbol{k}|^2$.

Following the theoretical model proposed in Gaster (1975), the model for a single three-dimensional WP source in non-parallel shear flow is given by

$$u_{WP}(x, y_0, z, t)$$

$$= A(y_0) \, \text{Re} \left\{ x^{-1/4} \sum_{\omega_n=\omega_0}^{\omega_N} \sum_{\beta_k=\beta_0}^{\beta_M} \exp i \left[\int_{x_0}^{x} \alpha(\zeta, \beta_k, \omega_n) \, d\zeta + \beta_k(z - z_0) - \omega_n t \right] \right\}, \tag{4.7}$$

where $u_{WP}(x, y_0, z, t)$ is the streamwise velocity of the WP at a given wall-normal height y_0, (x_0, z_0) is the location where the WP source is generated and (x, z) is the location where the WP source is measured. In our case of flow over a flat plate, the origin of the x axis is at the plate's leading edge. The term $x^{-1/4}$ has been included to compensate for the slight divergence of the mean flow (a model that accounts for downstream eigenfunction variation is provided in Cohen (1994)). Under the parallel flow assumption, we obtain

$$u_{WP}(x, y_0, z, t) = A(y_0) \, \text{Re} \left\{ \sum_{\omega_n=\omega_0}^{\omega_N} \sum_{\beta_k=\beta_0}^{\beta_M} \exp\{i[\alpha_{x_0,\omega_n,\beta_k}(x - x_0) + \beta_k(z - z_0) - \omega_n t]\} \right\}. \tag{4.8}$$

Here, the eigenvalue α_{x_0} associated with ω_n, β_k is kept constant along the streamwise direction. The model presented in (4.8) is a simplified version of the theoretical model proposed in Gaster (1975) and Cohen (1994). Its simplicity notwithstanding, this model provides estimates of the development of a WP disturbance over the relatively short distances between the sensors that are adequate for testing the performance of our DUET-based method prior to proceeding to experimental studies.

4.2. *Using LST to model sensor measurement*

We implement the LST model under the parallel flow assumption for generating simulated mixtures of N_s disturbance sources that are measured by N_x sensors. The disturbances considered comprise TS wave sources and WP sources. In the case of a single TS wave disturbance measured at a specific wall-normal height y_0, (4.1) can be written as

$$q(x, y_0, z, t) = |\hat{q}(y_0)| \, e^{-\alpha_{im}x} \cos(-\omega t + \phi_t(x, y_0, z)). \tag{4.9}$$

In (4.9) the phase shift in time, ϕ_t, at y_0 is determined by the spatial parameters of the disturbance

$$\phi_t(x, y_0, z) \triangleq \alpha_r x + \beta z + \phi(\hat{q}(y_0)) + \phi_{t_0}, \tag{4.10}$$

where ϕ_{t_0} is the initial phase and (x, z) are the current location coordinates.

927 A4-14

A source is defined as the signal that would have been measured by a sensor if all other sources were nil (that is, when no other mechanically generated signal is sensed). Each source is generated by a particular physical disturbance generator, which characterizes its signature in the sensor recordings. The source s_j is defined by its frequency ω_j and the initial phase ϕ_{t0_j} it had at its introduction location $\boldsymbol{r}_{s_j} = [l_x \ \ l_z]_{s_j}$ on the x–z plane. Let $\boldsymbol{r}_{x_i} = [l_x \ \ l_z]_{x_i}^\mathrm{T}$ be the location of sensor i on the x–z plane, where x_i stands for the signal measured by that sensor.

Using (4.9) and (4.10), we represent the measurement of source s_j by sensor i as

$$s_{ij} = |\hat{q}_j([l_y]_{x_i})| \, \mathrm{e}^{-\alpha_{im_j}([l_x]_{x_i} - [l_x]_{s_j})} \cos(-\omega_j t + \phi_{t_{ij}}), \tag{4.11}$$

where $\phi_{t_{ij}}$, the phase of source s_j as measured by sensor i, is given by

$$\phi_{t_{ij}} = \alpha_{r_j}([l_x]_{x_i} - [l_x]_{s_j}) + \beta_j([l_z]_{x_i} - [l_z]_{s_j}) + \phi_j([l_y]_{x_i}) + \phi_{t0_j}. \tag{4.12}$$

In (4.12), $[l_x]_{x_i} - [l_x]_{s_j}$ and $[l_z]_{x_i} - [l_z]_{s_j}$ are the downstream and spanwise distances, respectively, that the disturbance s_j travels from its generation point to sensor i. The variation in the phase of source s_j at the recording location of sensor i is due to the spatial wavenumbers α_{r_j}, β_j, and the eigenvector phase $\phi_j(y)$ of the source s_j at the vertical location $[l_y]_{x_i}$ of sensor i.

Similarly, for a WP source generated at $\boldsymbol{r}_{s_j}$ and measured by sensor i, we have

$$s_{ij} = \mathrm{Re} \left\{ \sum_{\omega_n=\omega_0}^{\omega_N} \sum_{\beta_k=\beta_0}^{\beta_M} \exp\{\mathrm{i}[\alpha_{x_{s_j},\omega_n,\beta_k}([l_x]_{x_i} - [l_x]_{s_j}) + \beta_k([l_z]_{x_i} - [l_z]_{s_j}) - \omega_n t]\} \right\}. \tag{4.13}$$

Finally, the source mixture measured by sensor i in the presence of N_s sources is

$$x_i = \sum_{j=1}^{N_s} s_{ij}, \quad i = 1, 2, \ldots N_x. \tag{4.14}$$

Equation (4.14) provides a general model for a system consisting of N_x sensors measuring N_s TS and WP disturbance sources, represented by (4.11) and (4.13), respectively.

4.3. *Numerical settings and procedure*

The dispersion relation is solved for α and q for the given frequency ω, spanwise wavenumber β, Reynolds number Re and base flow velocity profile $U(y)$ of BBL under the quasi-parallel flow assumption. We consider air flow at room temperature with kinematic viscosity $\nu = 0.15 \times 10^{-4}$ m^2 s^{-1}, and the free-stream velocity is set to $U_\infty = 5$ m s^{-1}. The disturbance sources are introduced at various downstream locations ($\boldsymbol{r}_{s_j}$) with various frequencies. Each given pair of frequency and downstream injection location of each source is associated with the corresponding non-dimensional frequency ω and the local Reynolds number, which is based on the local displacement thickness, i.e. $Re(x) = U_\infty \delta_d(x)/\nu$ (for BBL the displacement thickness is given by $\delta_d(x) = 1.7208\sqrt{\nu x/U_\infty}$). These are used to solve the dispersion relation for the spatial case. The sensors are set to measure the streamwise component of the flow, u. The obtained eigenvalues α and eigenfunctions $\hat{u}$ are used as inputs to the truth model, which consists of simulated source mixtures, measured by the sensors in the LST model. The simulations are performed

in dimensional form, where the dimensionless parameters ω and α of each source are dimensionalized using the local displacement thickness at the injection location of the source and U_∞. For simplicity and clarity of exposition, the non-parallel effect is neglected in our truth model, where it is assumed that the source eigenvalues and eigenfunctions remain unchanged during their downstream propagation towards the sensors. In reality, the non-parallel effect may significantly modify the amplitudes and phases of the sources at the location of the sensor, if the sources travel a long distance (many wavelengths) from their respective injection locations to the sensor. Nevertheless, the downstream distance between two neighbouring sensors, a key variable in the DUET method, is extremely small, compared with the disturbance wavelength. Therefore, the non-parallel effect is deemed negligible in our study, which is aimed at demonstrating the viability of the DUET method.

4.4. *The DUET settings*

The signals are acquired at a 1 kHz sample rate. In order to apply DUET to the two measured mixtures, we set the initial values of the DUET parameters for flow measurements according to those recommended for speech mixtures by Rickard (2007).

(i) *Window size.* The window size of the short Fourier transform is set to 256 ms. The window size is important for good DUET performance and description of the frequencies in the flow. Increasing the window size will result in good frequency localization in the time–frequency domain, but the time localization will deteriorate. Too narrow a window size will result in a poor frequency resolution, but will increase the time resolution. In Rickard (2007), it was found that speech is most window-disjoint orthogonal when a window of 1024 samples is used, corresponding to a length of 64 ms. In our study of shear flows, we found that good window sizes appropriate for time scales in our measurements are of 128–512 ms in length, corresponding to 128–512 samples at 1 kHz sample rate. This range results in a trade-off between frequency and time resolution (128 samples in favour of time resolution and 512 samples in favour of frequency resolution).

(ii) *Histogram domain.* The histogram domain $I(\alpha, \delta)$ is divided into 105 bins by 150 bins. The smoothing resolutions (Δ_α and Δ_δ) are set such that the weighted clusters of peaks that emerge on the histogram domain, centred on the actual mixing parameter pairs, are smoothed with a 3-by-3 neighbouring-bins window. This facilitates determination of localized histogram peaks.

(iii) *Histogram weights.* Motivated by the maximum-likelihood symmetric attenuation estimator in Yilmaz & Rickard (2004), we set $p = 1$ and $q = 0$. Good DUET performance is also obtained by setting $p = 2$ and $q = 0$, to reduce delay estimator bias (Yilmaz & Rickard 2004).

Next, two numerical examples are presented to study DUET performance when using various sensor configurations in various source mixing scenarios. The first example, which addresses five two-dimensional sources with two sensors placed at different heights, tests DUET as a source separation method. The second example, which addresses three three-dimensional sources with different propagation directions, sampled by a configuration of three sensors sharing the same height, tests the method's performance on each separated source.
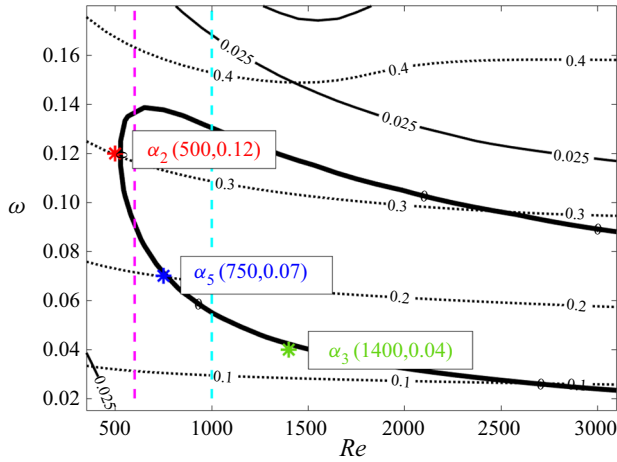
927 A4-16

Figure 5. Truth-model sources. WP sources s_1 (magenta dashed line) and s_4 (cyan dashed line) at specific Re; TS source eigenvalues, denoted by asterisk symbols: $\alpha_{s_2} = 0.3014 + 0.0006\mathrm{i}$ (red), $\alpha_{s_3} = 0.1347 + 0.0009\mathrm{i}$ (green) and $\alpha_{s_5} = 0.2010 + 0.0002\mathrm{i}$ (blue) at specific (Re, ω). Sources plotted over contours of constant streamwise wavenumber α_r (dotted black contours), growth rate α_{im} (solid black contours). The neutral curve is denoted by the bold black contour.

4.5. *Example 1: disturbance mixture separation*

This example serves to test and demonstrate the capabilities of DUET as a source identification and separation method in boundary layer measurement applications. To this end, our truth model comprises a five-source mixture, introduced upstream of the sensors. In particular, s_1 and s_4 are two-dimensional WPs introduced at downstream locations $x = 0.36$ m and $x = 1.0$ m (recall that the origin, $x = 0$, is located at the plate's leading edge). These locations correspond to Reynolds numbers $Re_1 = 600$ and $Re_4 = 1000$, respectively. The sources s_2, s_3 and s_5 are two-dimensional TS waves, introduced at downstream locations $x = 0.25$ m, $x = 2$ m and $x = 0.57$ m, corresponding to $Re_2 = 500$, $Re_3 = 1400$ and $Re_5 = 750$, respectively. The TS source dimensionless frequencies are $\omega_2 = 0.12$, $\omega_3 = 0.04$ and $\omega_5 = 0.07$, corresponding to 63.7, 7.6 and 24.8 Hz, respectively. The stability properties of the sources are illustrated in figure 5.

The sensors are located at $[l_x]_{x_1} = 2.29$ m and $[l_x]_{x_2} = [l_x]_{x_1} + 0.005$ m. The downstream separation of 0.005 m between the sensors is chosen to satisfy the fourth underlying assumption of the DUET method. Accordingly, figure 5 shows that the slowest TS disturbances propagate at a velocity of approximately $(c_r)_{max} \approx 0.3U_\infty$, and the maximal frequency in the simulated mixture (see figure 7), associated with TS source s_2, is $f_m = f_2 = 63$ Hz. Using (2.6) yields $|[l_x]_{x_1} - [l_x]_{x_2}| < \pi c_r/\omega_m = 0.3U_\infty/2f_m \approx 0.0118$ m, rendering an upper bound on the limiting distance between the sensors. We place each sensor at a different height above the plate: sensor 1 at 2 mm and sensor 2 at 1.4 mm. The simulated TS eigenfunction profiles (amplitude and phase of the streamwise disturbance velocity) are shown in figure 6, where the sensor positions are indicated by the horizontal lines (near the inner maximum of the streamwise component of the TS disturbance profiles).

Figures 7(*a*) and 7(*d*) display the outputs of two sensors that are used to measure the streamwise velocity component over a 2 s time interval. The corresponding Fourier transforms are shown in figures 7(*b*) and 7(*e*), and the spectrograms of the mixtures are shown in figures 7(*c*) and 7(*f*), respectively. Examination of figures 7(*b*) and 7(*e*) reveals
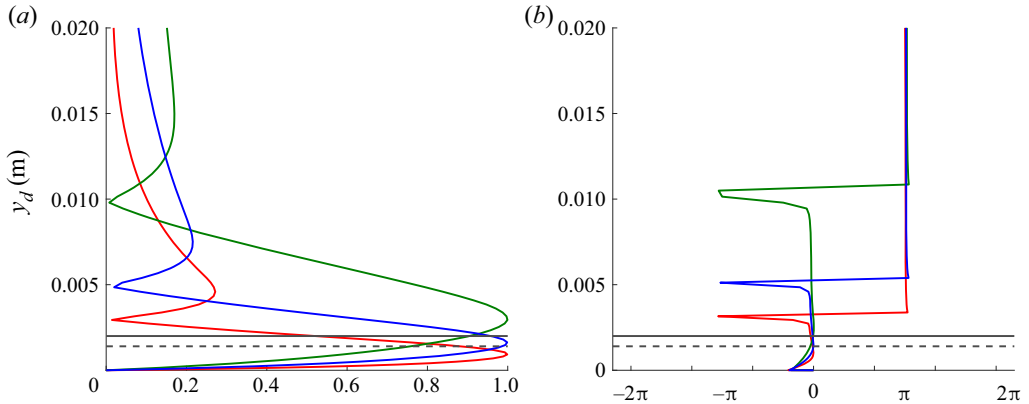
Figure 6. Streamwise component (u) of the three TS sources: s_2 (red), s_3 (green) and s_5 (blue). (*a*) Eigenfunction amplitude (normalized by its maximum) and (*b*) eigenfunction phase. Black lines: height of sensor 1 (solid) and sensor 2 (dashed). The sensor heights are related to the correct positions at the eigenfunction profiles of the sources by rescaling the y axis with the average δ_d of all injection locations of the TS sources.
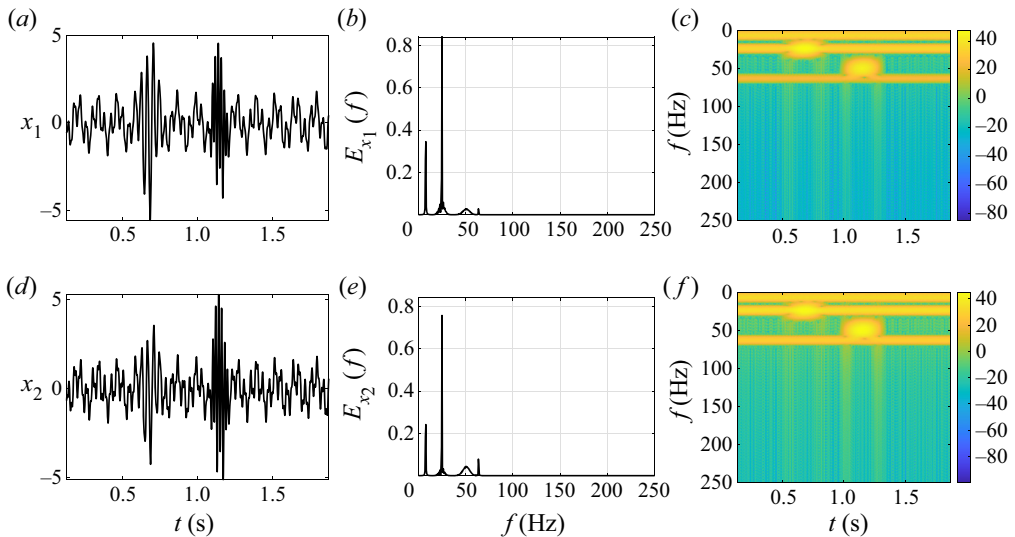

Figure 7. True (LST-computed) mixtures as measured by two sensors: (*a*) x_1 and (*d*) x_2. Corresponding Fourier transforms: (*b*) E_{x_1} and (*e*) E_{x_2}. Absolute values of windowed Fourier transforms (spectrograms), for which a window of 256 samples is used: (*c*) $20\log(|\hat{x}_1| + 10^{-6})$ dB and (*f*) $20\log(|\hat{x}_2| + 10^{-6})$ dB.

that each measured mixture contains the frequencies of the introduced sources. Each TS source has a unique single frequency, whereas the WP typical spectrum looks like a bell-shaped signature centred about a dominant frequency of around 50 Hz for s_1 and 24 Hz for s_4. Figures 7(*c*) and 7(*f*) demonstrate that the second DUET assumption (WDO) is not fully satisfied. Specifically, the WP source s_1 and the TS source s_2 co-dominate the flow for a certain time–frequency range. Similarly, but to a lesser degree, the WP source s_4 and the TS source s_5 coexist for a certain time–frequency range.

Figure 8 shows that the DUET-based method successfully identifies the correct number of sources. The isometric view of the histogram, presented in figure 8(*b*), shows five
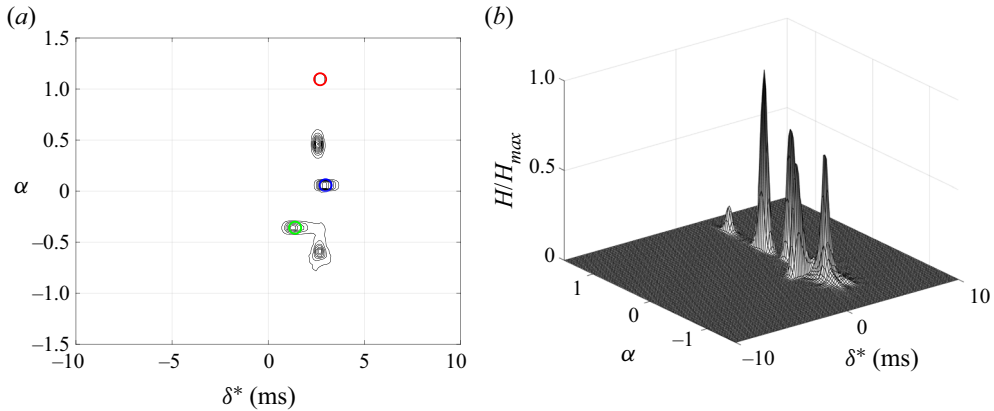
Figure 8. A DUET two-dimensional cross power weighted ($p = 1, q = 0$) histogram of symmetric attenuation $\alpha = (a - 1/a)$ and delay estimate pairs from two mixtures of five sources. (*a*) Contour plot (black) of the two-dimensional histogram with corresponding true (LST-computed) mixing parameter pairs for each TS source: s_2 (red), s_3 (green) and s_5 (blue). (*b*) Isometric view.

peaks associated with five true sources. Three peaks are related to the three TS sources and the other two peaks are associated with the WP sources. Figure 8(*a*) displays the mixing-parameter pairs of the true (LST-computed) TS sources, together with the peak contours. Clearly, three of the histogram peaks coincide with the mixing parameters of the true TS sources, s_2, s_3 and s_5. The other two peaks are associated with the WP sources, s_1 and s_4. In this example, histogram peaks are clustered around similar values of δ. The height difference between sensors has a strong effect on the α parameter. Thus, placing the sensors at different heights increases the scatter along the α axis, which facilitates distinguishing between the histogram peaks.

Obtained from the histogram peak locations, the identified mixing parameters are used to demix the sources. Figure 9 shows five estimated sources, denoted by $y_j, j = 1, 2, 3, 4, 5$, as identified by the DUET method. Figures 9(*a*) and 9(*j*) depict the time signatures of the estimates of sources s_1 and s_4, clearly featuring typical WP structures. Nonetheless, figure 9(*l*) shows that the estimate of WP source s_4 contains a weak spurious signal at 50 Hz. This frequency is also shared by TS source s_5. Figure 9(*m–o*) shows that the spectrum of the estimate of TS source s_5 is not contaminated by the estimates of other sources. However, it is attenuated in the region where WP source s_4 is active. Figure 9(*g–i*) indicates that the estimate of TS source s_3 contains very weak signatures (50 dB) of s_4, which do not affect its time signature. In this example we verified that multiple WP and TS disturbance sources in shear flows (sufficiently) satisfy the WDO condition, thus allowing accurate mixing parameter estimation with only two sensors, which yields high-fidelity signal recovery using DUET.

4.6. *Example 2: disturbance velocity estimation*

This example is used to demonstrate how our DUET-based method can be used to estimate the propagation velocity of disturbances in the flow using only three sensors, appropriately placed in the flow field. As in the previous example, LST is used for generating a truth model comprising a mixture of three sources: two three-dimensional TS (oblique) waves and one two-dimensional WP source. The three disturbance sources are introduced at
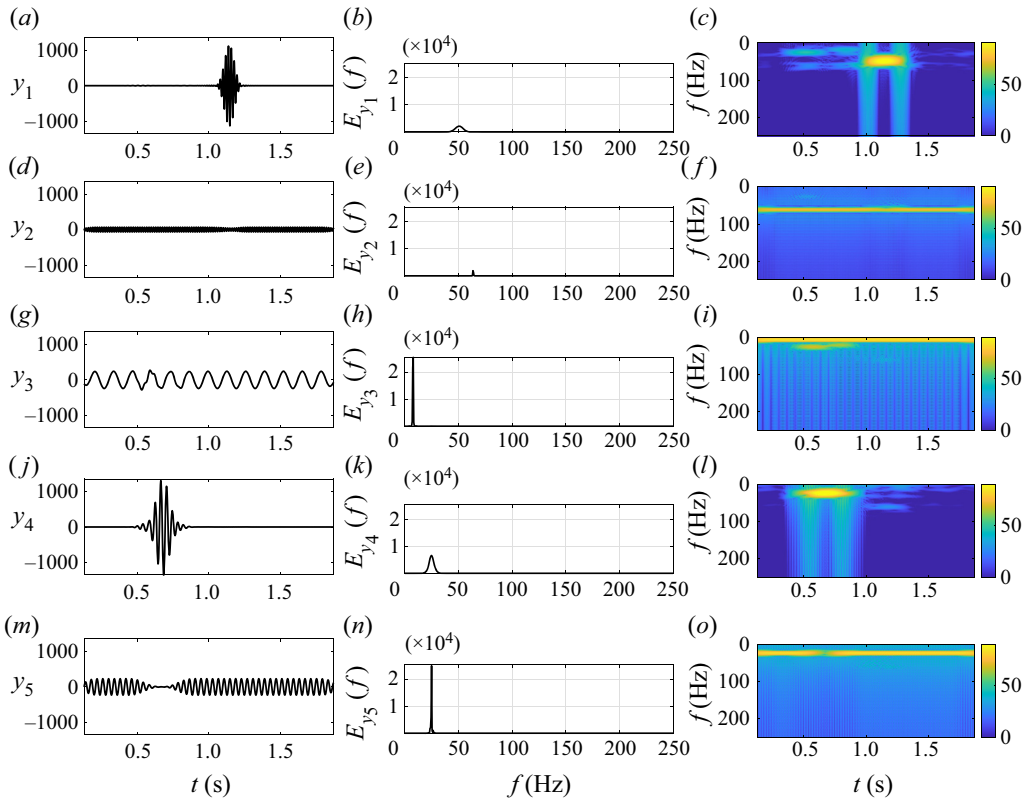
Figure 9. The DUET estimates of sources: (*a*) y_1, (*d*) y_2, (*g*) y_3, (*j*) y_4 and (*m*) y_5. Corresponding Fourier transforms: (*b*) E_{y_1}, (*e*) E_{y_2}, (*h*) E_{y_3}, (*k*) E_{y_4} and (*n*) E_{y_5}. Corresponding spectrograms (dB): (*c*) $|\hat{y}_1|$, (*f*) $|\hat{y}_2|$, (*i*) $|\hat{y}_3|$, (*l*) $|\hat{y}_4|$ and (*o*) $|\hat{y}_5|$.

Source	Source type and parameters	Injection location, downstream from leading edge (m)	Reynolds number, corresponding to injection location
s_1	Two-dimensional WP ($\beta = 0$)	0.15	385
s_2	Three-dimensional TS wave, $\omega_2 = 0.12$, $\beta_2 = 0.15$	0.365	600
s_3	Three-dimensional TS wave, $\omega_3 = 0.06$, $\beta_3 = -0.15$	0.5	700

Table 1. Disturbance sources.

different locations upstream of the sensors, as detailed in table 1, which also lists the source parameters.

The frequencies of the TS sources s_2 and s_3 are 53.1 and 22.7 Hz, respectively. Their corresponding eigenvalues are obtained by solving the dispersion relation for the spatial case, which results in $\alpha_2 = 0.2987 + 0.0003\mathrm{i}$ and $\alpha_3 = 0.1613 + 0.0039\mathrm{i}$.
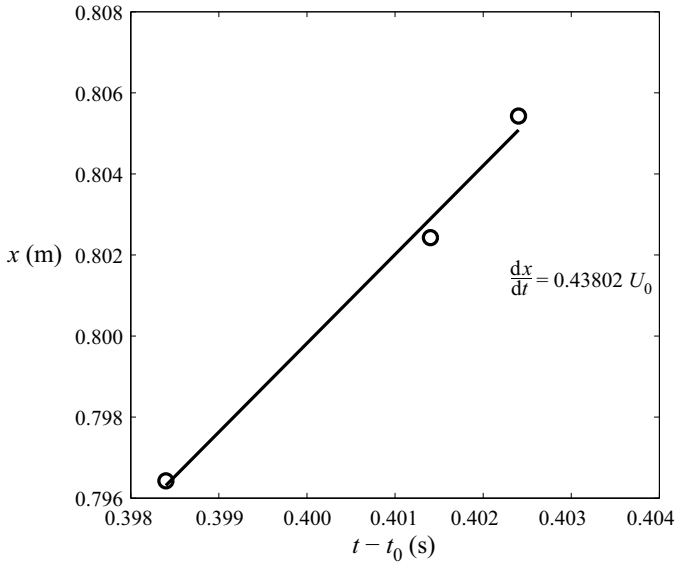
Figure 10. Plot of $\arg\max|u_{WP}(t, L_x)|$ for each sensor on the t–x domain, where x is the distance from the leading edge and t_0 is the pulse start time. The slope of the fitted linear function represents the envelope velocity of the WP source.

The propagation angle of a TS source is given by

$$\theta = \arctan\left(\frac{\beta}{\mathrm{Re}\{\alpha\}}\right), \tag{4.15}$$

which yields $26.7°$ for s_2 and $-42.9°$ for s_3. The angle of the two-dimensional WP ($\beta = 0$) source s_1 is $0°$. The propagation velocities of the TS sources correspond to their phase velocities as given by (4.4) from which we obtain that the TS waves travel at speeds $c_2 = 1.7950$ m s^{-1} and $c_3 = 1.3618$ m s^{-1} along their respective wave vector directions. In the case of the WP source, each of its many modes propagates with its own phase velocity, which differs from those of the other modes, but all travel as a group of waves at a group velocity c_g, also known as the WP envelope velocity. This velocity can be obtained by monitoring the leading edge and the trailing edge of the WP envelope in the t–x domain (Gaster 1975). For $Re = 851$ it is shown in Gaster & Grant (1975) that the leading edge of a three-dimensional WP propagates at 0.44 of the free-stream value, whereas the trailing edge seems to exhibit some local transient behaviour near the source before settling down to a path with a slope of $0.36U_\infty$. In particular, figure 10 shows the velocity of the WP in our simulation. In this figure we denote the time when the maximum value of the envelope (maximum of $|u_{WP}(t, x)|$) occurs at each downstream location of the sensors. The slope of the linear function fitting the three points on the t–x plane represents the speed of the WP travelling in the streamwise direction, which, in our simulation, is 2.1901 m s^{-1}.

The sensors are located at $\boldsymbol{r}_{x_1} = [796,\ 0]$ mm, $\boldsymbol{r}_{x_2} = [[l_x]_{x_1} + 6,\ 5]$ mm and $\boldsymbol{r}_{x_3} = [[l_x]_{x_1} + 9,\ 5]$ mm. They are placed at the same height above the plate, near the outer maximum of the streamwise component of the TS disturbance profiles.

The eigenfunction profiles (amplitude and phase of the streamwise disturbance velocities) of the two TS waves are shown in figure 11, where the sensors' height above the plate is indicated by the horizontal line. As demonstrated in figure 11(b), each TS source has a vertical phase profile, with two distinct regions (near and away from the surface)
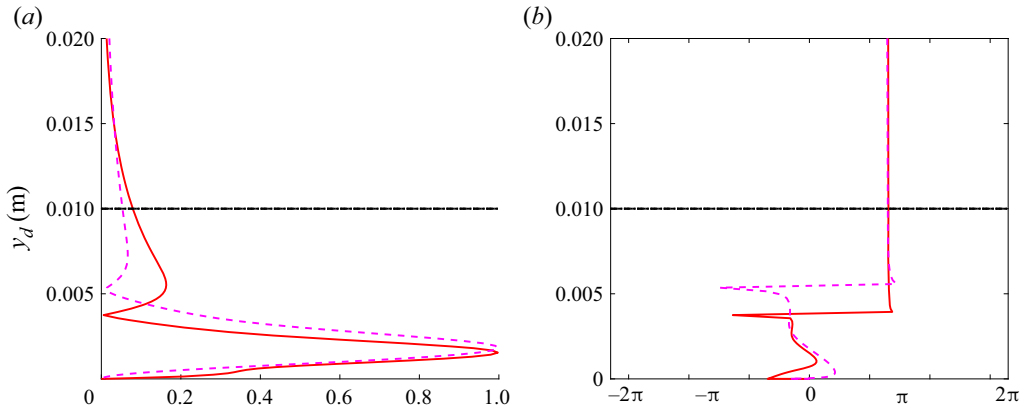
Figure 11. Streamwise component (u) of TS sources: s_2 (red) and s_3 (magenta). (*a*) Eigenfunction amplitude (normalized by its maximum) and (*b*) eigenfunction phase. The sensors' vertical position is denoted by the horizontal black dashed line.

separated by a jump with a value of π. This jump occurs approximately between the inner and outer maximum of the eigenfunction amplitude profile (figure 11*a*).

The phase profile of each source can result in false velocity angle estimation, because the phase change between the sensors is attributed to the source's horizontal propagation behaviour in our modelling framework. To overcome this problem, the sensors should be placed either (1) at the same height, outside or inside the boundary layer, e.g. near the inner maximum of the disturbance streamwise velocity profile (for non-parallel flow this height should be updated along the constant streamline), or (2) in the outer part of the boundary layer (if known *a priori*), possibly at different heights, where the phase profile is constant.

Using DUET for disturbance velocity estimation, which is the focus of the present example, is a two-stage procedure, with the first stage consisting of disturbance separation and identification. Since the theory underlying this stage has been thoroughly exemplified via the previous example, we defer the details concerning this stage to Appendix A. Thus, in the following, we only address the results of the second stage of the velocity estimation procedure, relying on the results of the first stage as they are described in Appendix A.

In figure 12 we overlay the histogram obtained using sensors 1 and 3 (blue contours) over the histogram obtained using sensors 1 and 2 (black contours). As can be clearly observed, the blue contours are shifted to the right relative to the black ones, that is, $|\delta_{j12}| < |\delta_{j13}|$, which agrees with the position of sensor 3 being downstream of sensor 2.

Next, we use the source delays, estimated from both histograms, to evaluate the corresponding velocity vector magnitude and direction by applying the method described in § 3. The resulting estimates are compared with the true values graphically in figure 13 and numerically in table 2.

As can be observed, the estimated magnitudes and direction angles of the two TS sources are in excellent agreement with the true values, obtained via LST simulation, whereas the estimates corresponding to the WP source exhibit moderate errors. These estimation errors can be attributed, in part, to our choice to compare the estimates to the WP group velocity, because of its dispersive nature. Another factor that can contribute to the estimation errors is the smoothing resolution of the DUET histogram (Δ_α and Δ_δ), used in (2.17) to determine the mixing parameters. We tune this resolution so as to bear a negligible impact on the estimates of the magnitude and direction of the velocity vector.
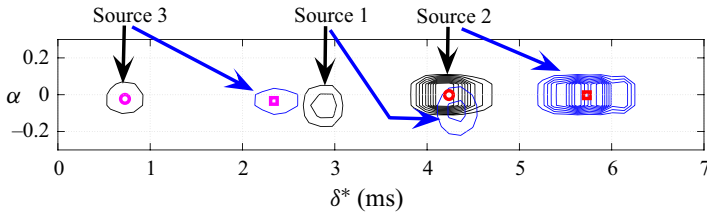
927 A4-22

Figure 12. Top view of DUET two-dimensional cross power weighted ($p = 1, q = 0$) histograms of symmetric attenuation ($\alpha = a - 1/a$) and delay estimate pairs. The histogram computed using sensors 1 and 3 (blue contours) is overlaid on the histogram computed using sensors 1 and 2 (black contours). The corresponding true (LST-computed) values of the mixing-parameter pairs of TS sources s_2 (red) and s_3 (magenta) are denoted by circles for sensors 1 and 2, and by squares for sensors 1 and 3. (For an isometric view and additional view angles, see figure 27 in Appendix A.).
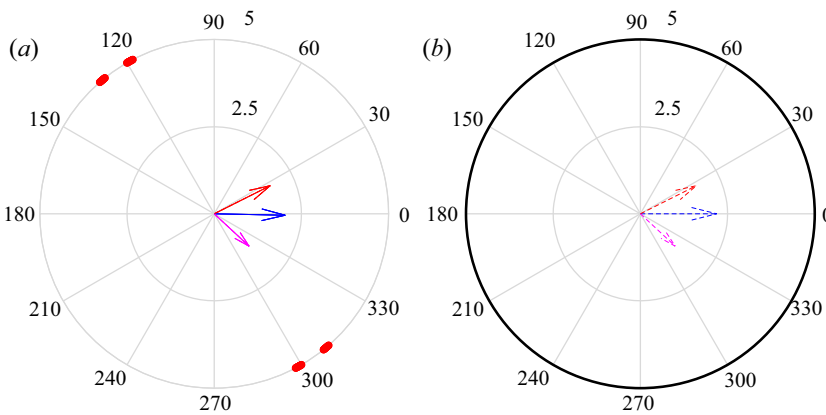
Figure 13. (*a*) The DUET-estimated versus (*b*) true (LST-simulated) source velocities (speeds in m s^{-1} and direction angles in degrees): s_1, blue; s_2, red; s_3, magenta. The regions of $\kappa(\mathbf{W}) > 50$ are denoted by red dots.

Source	s_1		s_2		s_3	
Speed (m s^{-1}), direction (deg)	u_1	θ_1	u_2	θ_2	u_3	θ_3
True	2.2	0	1.8	26.7	1.4	−42.9
Estimate	2.0	−1.2	1.8	26.7	1.4	−42.9

Table 2. Estimated versus true disturbance velocities.

5. Experimental study

We tested the method's performance using experimental data involving disturbance source mixtures in a boundary layer over a flat plate. The experiments were performed using a closed-loop wind tunnel at the Wind Tunnel Complex of Technion's aerospace engineering department. The tunnel has a concentration ratio of 5.76:1 and a test section cross-sectional area of 0.5 m by 0.5 m, and a length of 1.37 m. The plate dimensions are 0.45 m in width and 1.4 m in length. The trailing edge flap is 15 % of the total length of the plate. The free-stream velocity U_∞ is set in the range 4–5 m s^{-1}, the flow over the plate is laminar and the free-stream turbulence intensity level does not exceed 0.15 %. A single dielectric
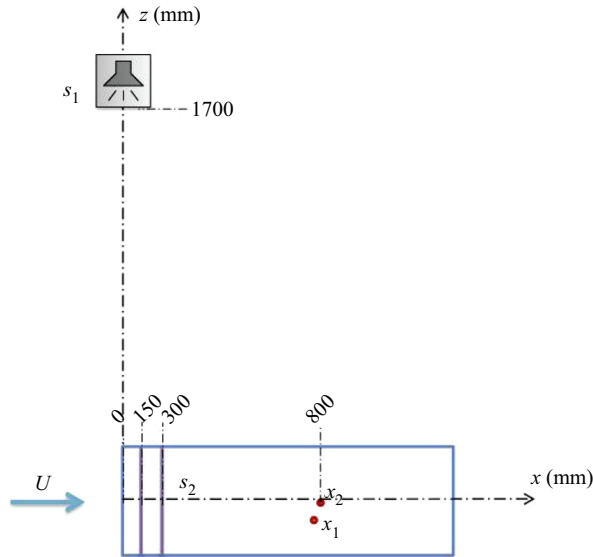
Figure 14. Flow over a flat plate with two disturbance generators: s_1 (loudspeaker source) and s_2 (plasma actuator source); and two hot-wire sensors: x_1 and x_2. Experimental set-up sketch.

barrier discharge (SDBD) plasma actuator (Moreau 2007; Corke, Post & Orlov 2009) and a loudspeaker are used for the generation of artificial disturbances. The streamwise velocity measurements above the plate are obtained with the aid of two hot-wire anemometers, which we set to acquire data over a 6 s time interval at a 5 kHz sampling rate. The measured signal is first preprocessed before applying the DUET method, to remove possible contamination from the mixtures resulting from free-stream turbulence, background noise and slow base flow variations. More details of the experimental set-up and the signal processing procedures are provided in Appendices B and C, respectively.

In what follows we present the results of two experiments. In the first we employ DUET to separate two disturbance sources using two sensors at different heights. The second experiment demonstrates how our DUET-based method, presented in § 2, can be used to estimate the velocities (magnitudes and directions) of mixed disturbance sources using a configuration of three sensors located at the same height.

5.1. *Experiment 1: blind disturbance separation with two sensors*

The set-up of the first experiment is shown in figure 14. An SDBD plasma actuator and a loudspeaker are used to generate two sources introduced upstream of the two hot-wire sensors, creating, in each sensor, a mixture comprising a TS wave and a WP. Specifically, placed outside the test section of the wind tunnel, the loudspeaker generates s_1, a single 60 Hz frequency disturbance (TS wave). Mounted on the plate 0.3 m downstream of the leading edge, the SDBD plasma actuator is used to generate s_2, a two-dimensional WP, being actuated via a 50 ms pulse signal. The free-stream velocity is set to 4.1 m s^{-1}. The sensors are positioned at 0.775 and 0.78 m downstream from the leading edge, with a 40 mm spanwise separation between them. Sensors 1 and 2 are placed at heights that correspond to $0.19U_\infty$ and $0.23U_\infty$, respectively (for sensor 2, this value is obtained at $y = 0.77$ mm).
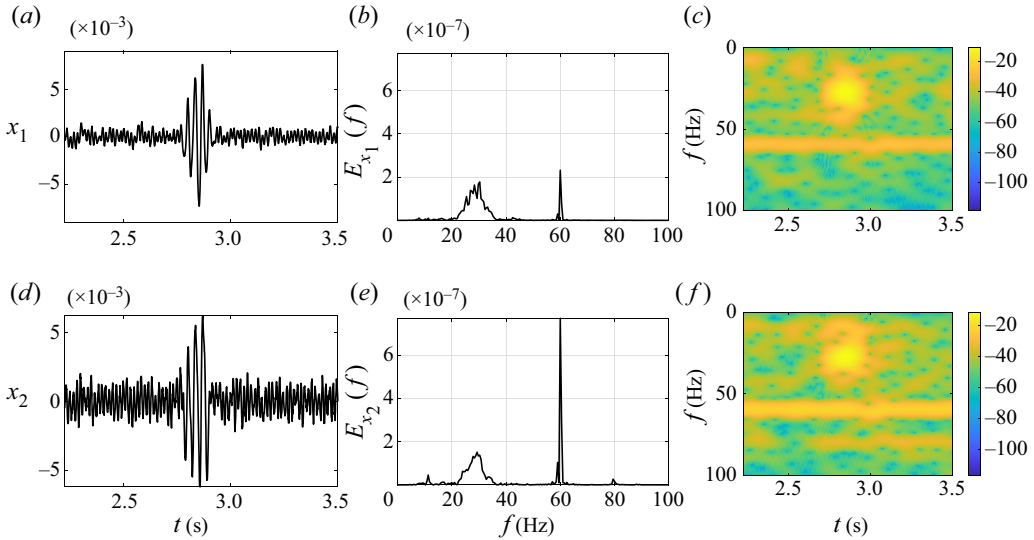
Figure 15. Mixtures as measured by two sensors: (a) x_1 and (d) x_2. Corresponding Fourier transforms: (b) E_{x_1} and (e) E_{x_2}. Corresponding spectrograms (dB), for which a window of 512 ms is used: (c) $|\hat{x}_1|$ and (f) $|\hat{x}_2|$.

Figures 15(a) and 15(d) display the streamwise velocity components, measured by two hot-wire sensors, after these signals are conditioned as described in Appendix C. The corresponding Fourier transforms are shown in figures 15(b) and 15(e), and the spectrograms of the mixtures are shown in figures 15(c) and 15(f), respectively. Figures 15(b) and 15(e) demonstrate that the dominant frequencies are, indeed, strongly related to the introduced sources. The bell-shaped signature of the WP has a dominant frequency of about 30 Hz, whereas the second source, generated by the loudspeaker, appears as a single-amplitude peak at 60 Hz. In addition, using a logarithmic scale in figures 15(c) and 15(f) reveals the weak presence of frequencies associated with experimental artifacts and the presence of noise in both mixtures. These were not removed by the signal preprocessing, because of their frequency-domain overlap with the sources comprising the mixture.

Figure 16 shows that the DUET-based method successfully identifies the correct number of introduced sources. The isometric view of the histogram, presented in figure 16(b), shows two peaks associated with two true TS and WP sources. Figure 16(a) displays the peak contours located around a mixing-parameter pair $(\alpha, \delta)_1 = (1.3, -3 \text{ ms})$, whereas the WP peak contours are located at $(\alpha, \delta)_2 = (-0.8, 3.5 \text{ ms})$. The estimated delay parameter of the WP source, along with the known sensor downstream position, enable finding the WP envelope velocity: $c_g \approx (l_{x_1} - l_{x_2})/\delta_2 = 5/3.5 = 1.43 \text{ m s}^{-1}$, which is $0.36U$, where U is the free-stream velocity. This result is in agreement with the analysis presented in (Gaster & Grant 1975), according to which the leading edge of the WP envelope in a BBL propagates at a velocity of $0.44U_\infty$, whereas the trailing edge of the envelope propagates at $0.36U_\infty$.

Obtained from the histogram peak locations, the identified mixing parameters are used to demix the sources. Figure 17 shows the two estimated sources as identified by the DUET method. Figures 17(a) and 17(d) clearly feature typical TS and WP time signatures, respectively. The noise, which is evident in the spectrograms of the measured mixtures in figure 15, is also evident in the spectrograms of the identified sources in figure 17. Nevertheless, the unique signature of each source is almost uncontaminated by that of
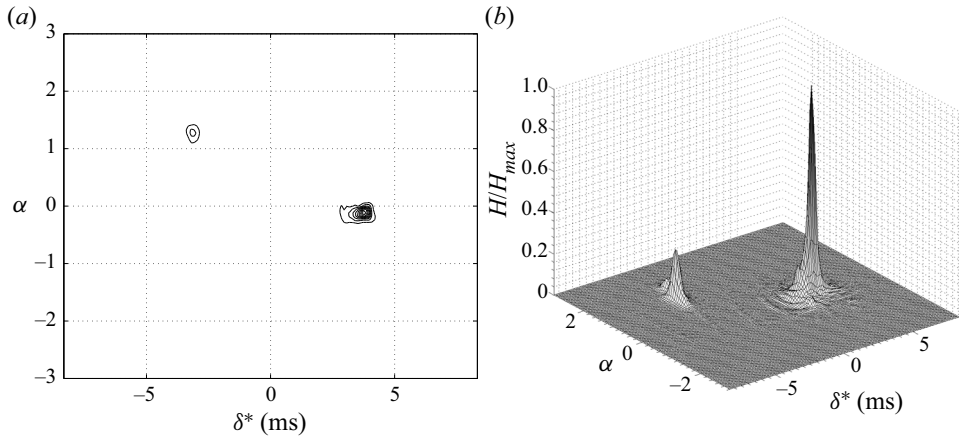
Figure 16. A DUET two-dimensional cross power weighted ($p = 1, q = 0$) histogram of symmetric attenuation $\alpha = (a - 1/a)$ and delay estimate pairs from two mixtures of two sources. (*a*) Contour plot of the two-dimensional histogram. (*b*) Isometric view.
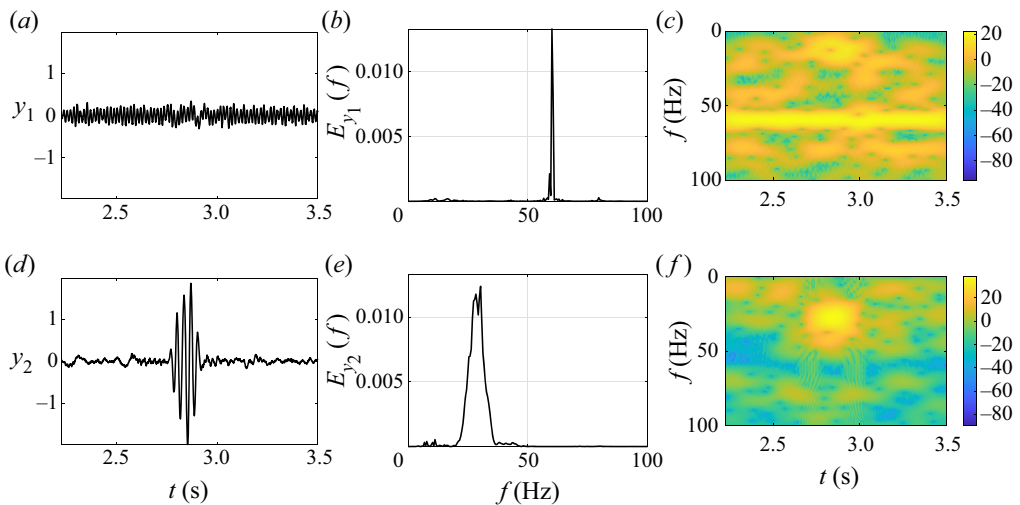

Figure 17. The DUET estimates of sources: (*a*) y_1 and (*d*) y_2. Corresponding Fourier transforms: (*b*) E_{y_1} and (*e*) E_{y_2}. Corresponding spectrograms (dB): (*c*) $|\hat{y}_1|$ and (*f*) $|\hat{y}_2|$.

the other source, indicating that the DUET method is robust with respect to low noise contamination levels that are hard to avoid in experiments.

This experimental example demonstrates that the DUET method performs well as a source identification and separation method, when applied to disturbances acting in a transitional boundary layer. We have obtained similar results in other experiments, under different mixing scenarios.

5.2. *Experiment 2: disturbance velocity estimation*

This experiment tests the performance of our DUET-based disturbance propagation velocity estimator. The experimental set-up is almost identical to the one described in § 5.1, except that, instead of using a loudspeaker, an additional plasma actuator is used
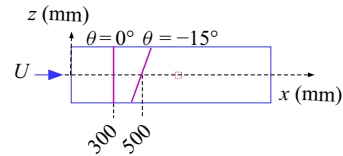
(*a*)
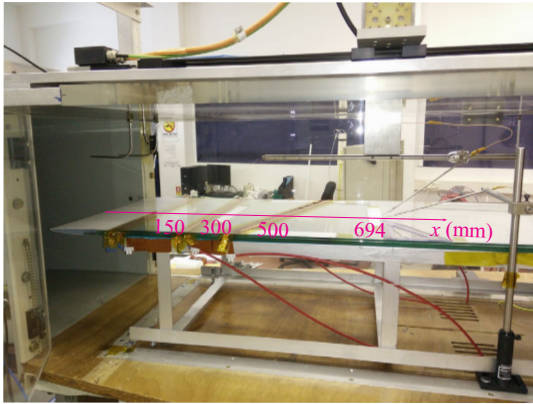
(*b*)

Figure 18. Experimental set-up of flow over a flat plate equipped with two active plasma actuators. (*a*) Photo of experimental set-up and (*b*) schematic diagram of experimental set-up. The region of the hot-wire sensors position is denoted by the magenta square.

to generate the second source, as depicted in figure 18. The two SDBD plasma actuators are mounted such that one is placed spanwise parallel to the leading edge and located at $x = 300$ mm downstream from the plate's leading edge, whereas the other is inclined at $15°$ to the leading edge, and its centre ($z = 0$ mm) is located at $x = 500$ mm. The inclined actuator can generate oblique TS wave or WP disturbances.

The two SDBD actuators are used to introduce two disturbances into the boundary layer. The plasma actuator parallel to the leading edge is used to generate s_1, a two-dimensional WP source, travelling downstream at $\theta = 0°$ (so that $\beta_0 = 0$, by (4.15)). The inclined plasma actuator is used to generate s_2, an oblique WP source, travelling downstream at $\theta \approx -15°$. Both actuators are driven by a single, 10 ms pulse, such that the actuator parallel to the leading edge is delayed by 10 ms with respect to the other, to render both sources distinguishable in the time–frequency domain. To ensure linear interactions, both actuators are driven by the smallest voltage that still generates uniform discharge along the actuator span.

The free-stream velocity U_∞ is set to $5\,\text{m s}^{-1}$. All sensors are placed at 0.5 mm height above the plate's surface, rendering a measured mean streamwise velocity of $0.27U_\infty$ at that height. Three sensor configurations, shown in figure 19 and termed 'asymmetric', 'singular' and 'symmetric', are tested (see Appendix B.4 for the technique used to realize a three-sensor configuration using only two hot wires). In each configuration the sensors are located at the central region of the plate, and the fixed sensor (sensor 1) is placed at $r_{x_1} = [643,\ 25]$ mm. The small variations in sensor pair locations between the configurations, as shown in figure 19, translate to different source arrival times at the sensors.

Typical mixtures, measured by sensors 1 and 3 in the asymmetric configuration, are shown in figure 20. The presence of both WP sources is evident in both measured mixtures. The corresponding DUET-estimated sources are shown in figure 21, which demonstrates effective source separation. Similar results, not shown here for conciseness, were obtained for the singular and symmetric sensor configurations.

For each of the three sensor configurations, we overlay, in figure 22, the histogram obtained by using sensors 1 and 3 (blue contours) on the histogram obtained by using sensors 1 and 2 (black contours). As can be clearly observed, the black contours are shifted
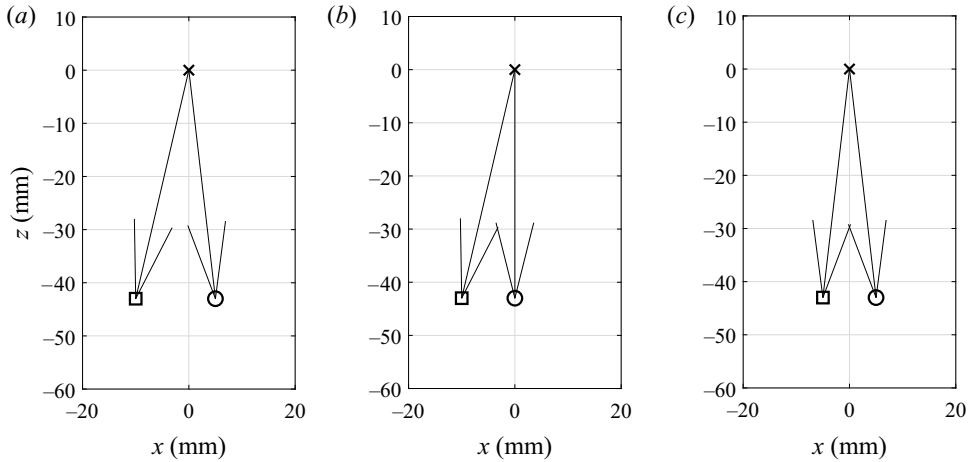
Figure 19. Top (*x–z* plane) view of three studied sensor configurations relative to $r_{x_1} = [643, \; 25]$ mm (at the origin). The sensors are denoted by symbols: ×, sensor 1 (master); circle, sensor 2 (slave); square, sensor 3 (slave). Baselines are denoted by arrows. (*a*) Asymmetric configuration, (*b*) singular configuration and (*c*) symmetric configuration.
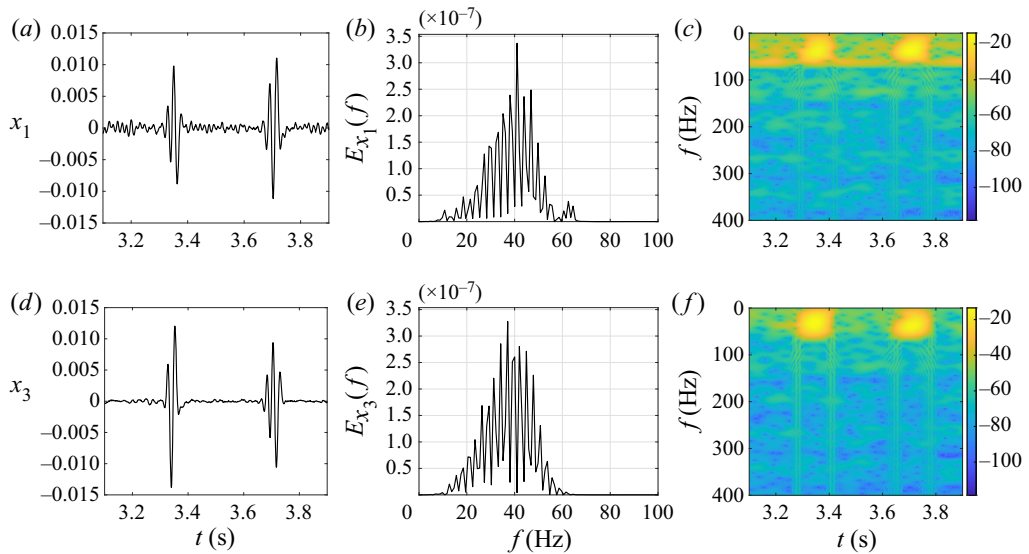

Figure 20. Mixtures as measured by two sensors for the asymmetric configuration: (*a*) x_1 and (*d*) x_3. Corresponding Fourier transforms: (*b*) E_{x_1} and (*e*) E_{x_3}. Corresponding spectrograms (dB), for which a window of 128 ms is used: (*c*) $|\hat{x}_1|$ and (*f*) $|\hat{x}_3|$.

to the right relative to the blue ones, that is, $|\delta_{j13}| < |\delta_{j12}|$, which agrees with the position of sensor 2 being downstream of sensor 3 in all three configurations.

Next, we use the source delays, estimated from both histograms, to evaluate the corresponding velocity vector magnitude and direction by applying the method of § 3. These estimates are shown graphically in figure 23 and summarized numerically in table 3, for each of the tested sensor configurations.
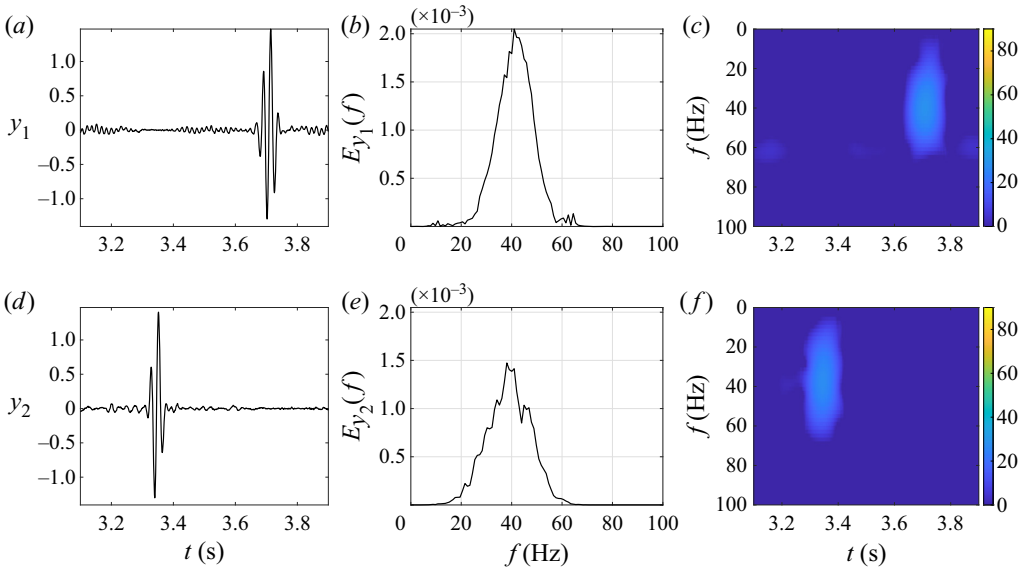
Figure 21. The DUET estimates of sources using sensors 1 and 3 in asymmetric configuration: (*a*) y_1 and (*d*) y_2. Corresponding Fourier transforms: (*b*) E_{y_1} and (*e*) E_{y_2}. Corresponding spectrograms (dB): (*c*) $|\hat{y}_1|$ and (*f*) $|\hat{y}_2|$.
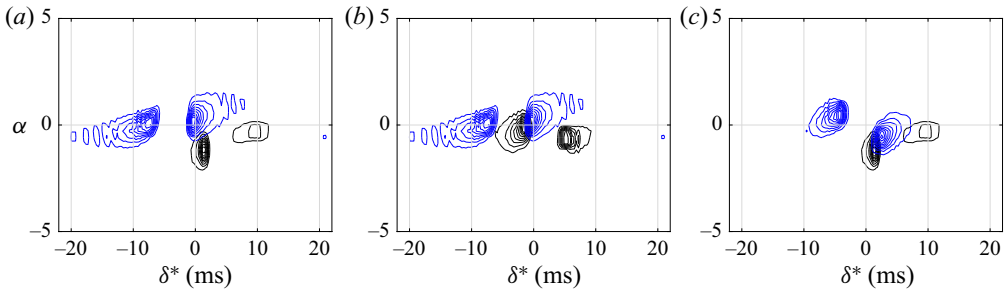

Figure 22. Top view of DUET two-dimensional cross power weighted ($p = 1$, $q = 0$) histograms for the studied three-sensor configurations. The histogram computed using sensors 1 and 3 (blue contours) is overlaid on the histogram computed using sensors 1 and 2 (black contours). (*a*) Asymmetric configuration, (*b*) singular configuration and (*c*) symmetric configuration.
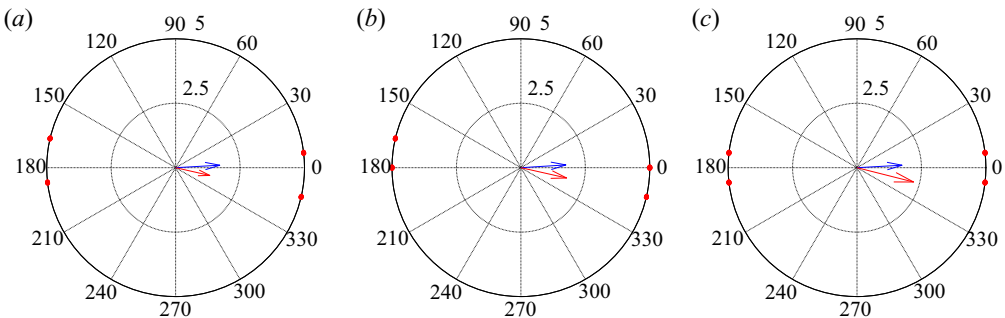

Figure 23. Estimated velocities of sources s_1 (blue) and s_2 (red) using the three studied sensor configurations. (*a*) Asymmetric configuration, (*b*) singular configuration and (*c*) symmetric configuration. The regions of $\kappa(\boldsymbol{W}) > 50$ are denoted by red dots.

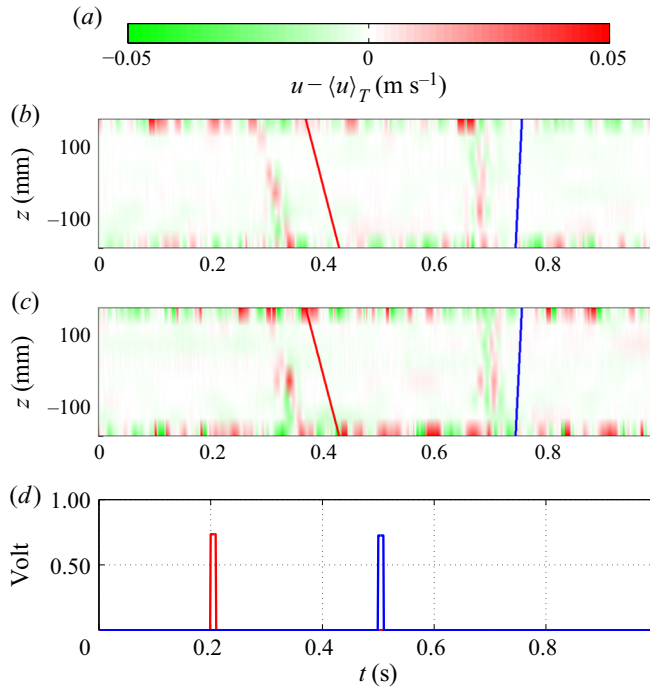| Source | Speed (m s^{-1}) | Configuration | | |
	Direction (deg)	Asymmetric	Singular	Symmetric
s_1	u_1	1.72	1.75	1.75
	θ_1	3.20	3.52	3.13
s_2	u_2	1.36	1.82	2.26
	θ_2	-12.80	-12.70	-14.20

Table 3. Estimated source velocities.

Figure 24. Time histories of streamwise disturbance velocity at two downstream stations. (*a*) Colourbar for (*b,c*). Time history of streamwise disturbance velocity at (*b*) $y = 0.9$ mm, $x = 600$ mm and (*c*) $y = 0.9$ mm, $x = 650$ mm. (*d*) Pulsation sequence of actuator parallel to leading edge (blue) and inclined actuator (red). Free-stream velocity is $U = 5$ m s^{-1}. In (*b,c*) the estimated values of WP envelope inclination angles are denoted by the red (s_2) and blue (s_1) lines.

The results show that the streamwise-travelling two-dimensional WP disturbance is estimated quite consistently by all three sensor configurations. The oblique WP estimates, on the other hand, exhibit a substantially larger variation. Nevertheless, the estimated WP envelope velocities of both sources are between $0.3U_\infty$ and $0.45U_\infty$, which are close to the values of our numerical example (see § 4.6).

The discrepancy of about 3° between the estimated θ_1 and the 0° angle of the parallel actuator (that created it) can be attributed to several factors: (1) an imperfect alignment of the sensor on the x–z plane (the positioning accuracy was 1 mm), (2) random artifacts, caused by the fact that two repeated experiments had to be done to obtain the required three sensor measurements with only two sensors, (3) DUET histogram resolution (although this resolution was tuned to bear a negligible impact on the estimates of the velocity vector),
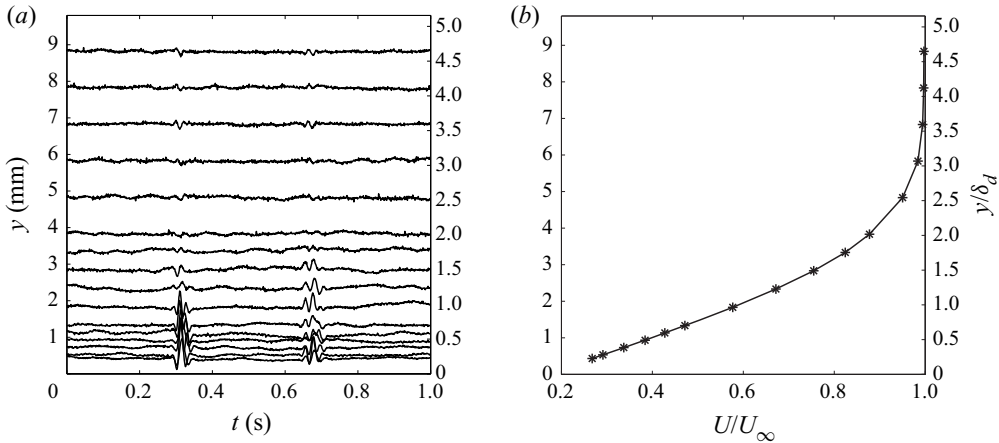
Figure 25. (*a*) Time history of disturbance streamwise velocity on the *t–y* domain and (*b*) mean flow profile without actuation, both obtained at $x = 600$ mm and $z = 0$ mm, for $U_\infty = 5$ m s^{-1}.

(4) the disturbance can, potentially, not precisely adhere to the inclination angle of its generating actuator when propagating downstream and (5) slight variations in the phase profiles may exist, in particular for the s_1 WP. In what follows, we examine the latter two factors in further detail.

To investigate how the generated disturbance changes its inclination angle as it propagates downstream from its generating actuator, we track the temporal evolution of a localized disturbance within the boundary layer over a flat plate. Figure 24 shows the time history of the streamwise velocity of the disturbances as they pass through two points, located at 600 and 650 mm from the leading edge, both at a height of $y = 0.9$ mm above the plate. Consisting of 10^3 points, the velocity record is digitized at 1 kHz, such that the total measuring time is 1 s for each (x, y, z) location. The measurement sequence is synchronized by a pulse from the computer that triggers the disturbance generator. The inclined actuator, which generates s_2, and the parallel actuator, which generates s_1, are triggered 0.2 and 0.5 s after the beginning of the recording, respectively. At each measuring point, an ensemble average of six realizations of the disturbance passage is computed (this number of realizations was found to be sufficient to adequately represent the flow structure).

In figure 24 the WP propagation angle at both measuring points is evident within the central region, where the boundary layer maintains its laminarity and is not affected by the spanwise edges of the plate. Assuming that the propagation angles remain fixed from disturbance generation until the mixtures reach the sensors, we use the estimated angles from table 3 to plot the estimated wavefront inclination angle in the *t–z* domain over the measured time history of the flow. As figure 24 clearly shows, the inclined WP source, s_2, is estimated very well, and better than the WP source s_1. This is most likely due to the phase changes of s_1 at the sampled locations.

To determine if there are slight variations in the disturbance phase profiles, we plot in figure 25(*a*) the same time histories used to obtain figure 24(*c*), on the *t–y* domain, at $x = 600$ mm and $z = 0$ mm. The free-stream velocity is $U = 5$ m s^{-1}. The signals are normalized by their maximal values to make them more pronounced. In figure 25(*b*) we show the mean profile of the flow without actuation at the same location, in order to reference the sensor heights to the canonical boundary layer at that location. Some slight non-coherence in the shape of source s_1 is evident below the height of 1 mm (which

is below $0.35U_\infty$), indicating disturbance phase variations at that region. Thus, placing sensors at that height reduces our method's precision in estimating the velocity vector of source s_1.

6. Concluding remarks

This paper presents a novel approach for the isolation and identification of disturbances in a boundary layer. Enabling this approach, the model adopted in this work regards the flow state as an unknown mixture of disturbance sources. The primary goal of the study is to identify the flow physics, or, in terms of our model, the mixing process, based on information acquired using a limited number of sensors embedded in the flow.

Because the number of disturbances and their mixing parameters in the boundary layer are *a priori* unknown, we use DUET as a BSS mechanism to reconstruct the separate sources and their mixing process. Only two sensors, as a minimum, are required for this source separation and identification, and this number is independent of the number of disturbances active in the flow. Adding an additional sensor, and complying with some physics-based design rules, we also present a method, motivated by techniques for GPS-based spacecraft attitude determination, to determine the propagation velocity vector (magnitude and direction) of each of the sources, based on readings of only three sensors appropriately positioned in the flow field.

We demonstrate our methods both numerically and experimentally. The numerical study employs LST to model the source mixtures acquired by sensors placed in a BBL. We consider three-dimensional TS waves and WPs, which may propagate downstream along with the free-stream direction or at a certain angle with respect to it. Carried out in a wind tunnel, the experimental study considers flow over a flat plate, with hot wires as sensors and a loudspeaker and plasma actuators as source generators.

Both numerical and experimental studies demonstrate the robustness of the DUET-based method with respect to the validity of its underlying assumptions. This is especially true in the experimental domain, where these assumptions are more challenging to satisfy, because of sensor positioning and alignment errors, random artifacts and measurement noises. In particular, we demonstrate how DUET can separate sources that coexist over some time–frequency interval, i.e. when the set-up does not fully comply with the source sparsity (WDO) assumption, which is one of DUET's underlying assumptions.

Our novel identification and isolation scheme may be used to provide new insights and perspectives on how transitional flows can be studied. The information gained concerning sources and their mixing parameters may provide essential insights into the physical fluid system, and information on aspects of the flow that can be relevant from control perspectives.
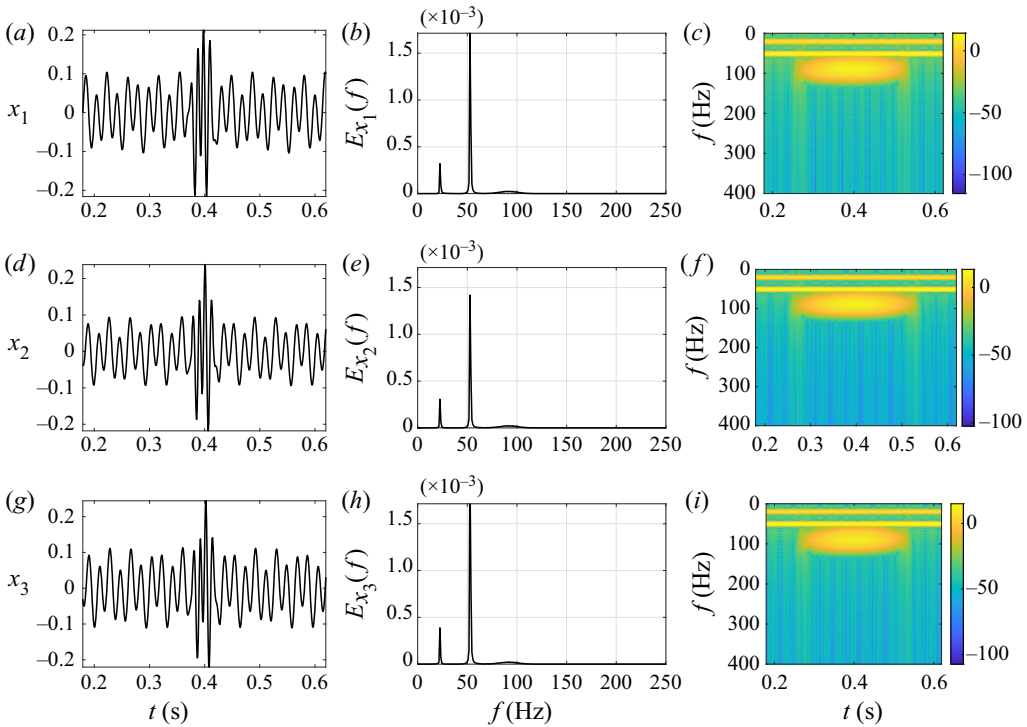
927 A4-32

Figure 26. Time signatures as measured by the three sensors: (*a*) x_1, (*d*) x_2 and (*g*) x_3. Respective Fourier transforms: (*b*) E_{x_1}, (*e*) E_{x_2} and (*h*) E_{x_3}. Respective spectrograms (dB): (*c*) $|\hat{x}_1|$, (*f*) $|\hat{x}_2|$ and (*i*) $|\hat{x}_3|$.

Author ORCIDs.

Ⓘ I. Gluzman https://orcid.org/0000-0002-9153-626X;

Ⓘ Y. Oshman https://orcid.org/0000-0001-9471-3789.

Appendix A. Disturbance separation with two sensors (example 2 in § 4.6)

In this appendix we provide details pertaining to the application of DUET for source separation in example 2 of § 4.6. Figures 26(*a*), 26(*d*) and 26(*g*) display the time behaviour of the mixtures over the time interval [0.2, 0.6] s. The corresponding Fourier transforms are shown in figures 26(*b*), 26(*e*) and 26(*h*), from which it can be seen that each mixture contains the frequencies of all introduced sources. Each TS source has a unique single frequency, whereas the WP spectrum exhibits a typical bell-shaped signature with a maximum at about 90 Hz. The respective spectrograms of the mixtures in the time–frequency domain are shown in figures 26(*c*), 26(*f*) and 26(*i*).

Figure 27 shows the histogram computed using the measurements of sensors 1 and 2. The isometric view of the histogram in figure 27(*b*) reveals three peaks associated with the three original sources: two TS sources and one WP source. In figure 27(*a*) we superimpose the mixing-parameter pairs of the TS sources, as computed by LST, over the histogram peak contours. Clearly, the histogram peaks coincide with the mixing parameters of the three LST-computed sources.

The identified mixing parameters, obtained from the histogram peak locations, are used to demix the sources. Figure 28 shows the three DUET-estimated sources. The quality of the separation is manifested by the fact that the signature of each estimated source is uncontaminated by the other two sources.
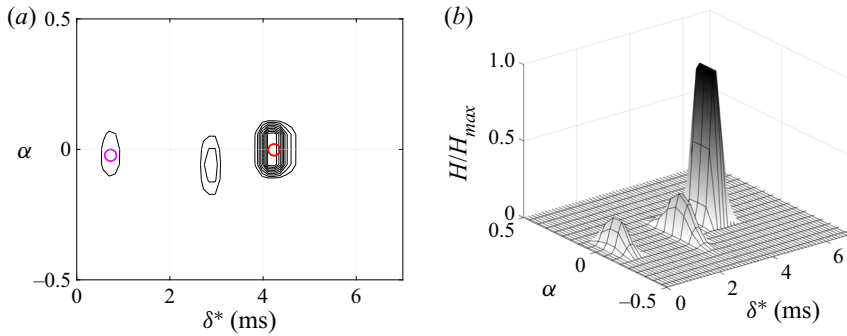
Figure 27. A DUET two-dimensional cross power weighted ($p = 1$, $q = 0$) histogram using sensors 1 and 2. (*a*) Contour plot (black) of the histogram with corresponding true (LST-computed) mixing-parameter pairs for each TS source s_2 (red circle) and s_3 (magenta circle). (*b*) Isometric view.
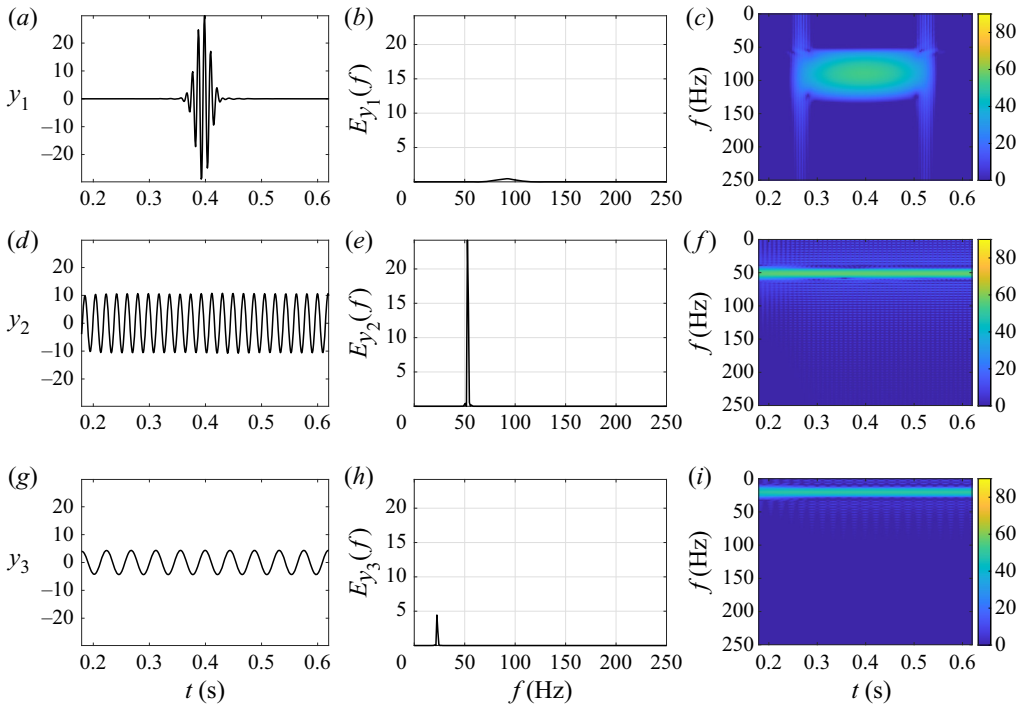

Figure 28. The DUET estimates of sources using sensors 1 and 2: (*a*) y_1, (*d*) y_2 and (*g*) y_3. Corresponding Fourier transforms: (*b*) E_{y_1}, (*e*) E_{y_2} and (*h*) E_{y_3}. Corresponding spectrograms (dB): (*c*) $|\hat{y}_1|$, (*f*) $|\hat{y}_2|$ and (*i*) $|\hat{y}_3|$ dB.

Appendix B. Experimental set-up and data processing details

In this appendix we briefly describe the components of the experimental set-up.

B.1. *Wind tunnel*

The experiments are performed in a closed-loop wind tunnel with a contraction ratio of 5.76:1, a test cross-sectional area of 0.5 m by 0.5 m and a length of 1.37 m. The sidewalls of the test section are made of 10 mm thick transparent Perspex, with an adjustable angle

to control the pressure gradient inside the test section. The air temperature is $20 \pm 2\,°$C. The air flow is driven by a vane-axial fan powered by a 15 kW motor, which is capable of generating a free-stream velocity up to $50\,\text{m s}^{-1}$ inside the test section. The tunnel is designed to have low turbulence levels ($0.15\,\%$ at velocities up to $10\,\text{m s}^{-1}$ for a filtered range of 0.1–500 Hz). These low turbulence levels are achieved by placing corner vanes at each corner of the tunnel, and by positioning a settling chamber upstream of the converging nozzle that contains a honeycomb with a cell diameter of 5 mm, and four screens downstream of it.

B.2. *Flat plate*

The boundary layer is formed along a flat plate made of three, combined, 4 mm thick glass sheets that satisfy a waviness criterion for plate surfaces used for stability experiments: $\varepsilon / \lambda_{TS} < 10^{-3}$, where ε is the height above the plate and λ_{TS} is the TS wavelength (Saric 2008). The leading edge has an asymmetric shape and is designed to minimize the adverse pressure gradient according to Fransson (2004). The trailing edge is equipped with a flap having an adjustable angle, that enables control of the stagnation line at the leading edge, thereby preventing boundary layer separation there. The plate dimensions are 0.45 m in width and 1.4 m in length. The trailing edge flap is 15 % of the total length of the plate. A filling material (plasticine) is inserted between the various parts (the leading edge, plate and trailing edge flap) and covered by a single layer of Kapton tape in order to avoid junction discontinuities. The plate is mounted on a supporting frame, specially designed to minimize the test section area blockage. The front tip of the plate's leading edge is placed at the beginning of the test section, and the plate's top surface is positioned at mid-height of the test section.

B.3. *Disturbance generators*

SDBD plasma actuators and a loudspeaker are utilized for generation of controlled disturbances. The actuation signals for both are generated with the aid of LabVIEW software. Plasma actuators have been studied and used in a wide range of flow applications. Detailed reviews of plasma actuator physics, experiments and applications are given in Moreau (2007), Corke *et al.* (2009) and Kriegseis, Simon & Grundmann (2016).

We use copper tape (66 µm thick and 10 mm wide) as the electrodes of the actuator, a glass sheet (4 mm thick) as the dielectric insulation between the electrodes and Kapton tape for encapsulation of the grounded electrode. The actuation signal is generated by a GBS MiniPuls 2.1 kit that consists of two boards: (1) a full-bridge converter and (2) a transformer cascade (RM14). The assembly can generate high AC voltages with frequencies in the range 5–20 kHz, and amplitudes up to 10 kV (7 kV$_{RMS}$). The system internal control allows adjusting the signal's burst frequency in the range 0–400 Hz, and has a duty cycle in the range 0 %–100 %.

A single DIBEISI difuzor loudspeaker, having a diameter of 200 mm, is used as an additional disturbance generator. The loudspeaker is placed outside the test section and away from the measuring system to prevent mechanical vibrations. The actuation input signal to the loudspeaker is a superposition of sine waves with maximum amplitudes of 3 V, amplified by a -10 dB gain via a MAX 860 power-amplifier capable of 300 W output. The generated acoustic waves create pressure disturbances that interact with the boundary layer.

B.4. *Sensors and data acquisition system*

The velocity of the free stream entering the test section is measured by a Pitot tube connected to an MKS BARATRON model 398HD pressure transducer, mounted on top of the mid-spanwise part of the test section inlet plane. The streamwise velocity (above the plate) is measured with the aid of two hot wires (DANTEC, type 55P11) connected to a hot-wire anemometry system of A. A. Lab Systems. The straight, 5 μm in diameter, tungsten hot-wire probes are kept at an overheat ratio of 1.6, corresponding to a maximal frequency response of 30 kHz. During calibration, each hot wire is placed adjacent to the Pitot tube. The calibration includes seven velocities in the range 0–10 m s^{-1} at a temperature of 20 °C. The hot-wire anemometer and BARATRON pressure transducer data acquisition are controlled using a regular PC and LabVIEW software.

During the measurement of the disturbance mixtures in the boundary layer, one hot wire is kept stationary, while the other is mounted on a three-axis traversing mechanism, with a resolution of 5 μm in the wall-normal vertical direction and 1 mm in both the streamwise and spanwise directions. The positioning of the probe within the boundary layer at a given downstream station is controlled by the computer that drives the stepping motors through LabVIEW software.

Our method requires the use of (at least) three sensors for reconstructing the velocity vectors of the sources. However, in our experiments, laboratory set-up limitations dictated the use of only a pair of hot wires. To circumvent this limitation, we used the following approach. One hot-wire sensor, designated as 'master sensor 1', was kept stationary throughout the entire experiment. The experiment was performed two times, where, in the first run, the traversed hot wire was used as 'slave sensor 2', in one location, and, in the second run, as 'slave sensor 3', in another location. This approach relies on the facts that (1) DUET can be used with only two sensors and (2) the initial phase of the sources in the mixture is irrelevant to our method. We assume that the mixing parameters (particularly the delay of arrival) of each source are the same between the repeated experiments. It should be noted, however, that this assumption can never be ideally realized in practice, so that the use of repeated experiments necessarily adversely affects the method's accuracy.

Appendix C. Signal preprocessing before applying DUET

Prior to applying our DUET-based method to the acquired signals, they are preprocessed according to the following consecutive steps.

   (i) Prior to recording the signals, hardware low-pass filtering is applied, so that the filtered signals have a cutoff frequency of 1 kHz. This is done to eliminate the effects of electromagnetic interference, which is generated by the SDBD plasma actuator. The selected cutoff frequency does not detrimentally affect the measurements because the relevant boundary layer frequencies in this study are below 200 Hz.
  (ii) Next, the signals are detrended to remove slow variations of the base flow with typical frequencies well below those of the introduced sources. Detrending is performed by subtracting from the signal a smoothed version of it, generated by applying a moving average operator to the measured signal. The smoothing window length of the moving average operator is set to smooth out short-term fluctuations of source mixtures and highlight the longer-term trends of the base flow. Detrending is done to ensure that the DUET-based method does not identify these slow variations as additional sources existing in the flow.

(iii) The detrended signals are then low-pass-filtered to remove artifacts and noise below 1 kHz that result from electrical devices, such as the traverse stepper motor noise and sensor noise, as well as from random flow events or truncation errors of the recorded signals. This procedure is done by applying to the recorded signal a moving average operator with a window length designed to ensure that the signal acquisition sample rate is as short as possible but sufficiently long to remove these artifacts.

(iv) Finally, we make sure that the detrended signals are centred by subtracting their computed means from them. This ensures the removal of the base flow profile effect on symmetric attenuation, which is based on the ratio between the absolute values of the sensor measurements. Therefore, by centring each measured signal, we ensure that the estimated symmetric attenuation would be within the predetermined limits of the DUET histogram, for appropriate source separation.

REFERENCES

AMITAY, M., TUNA, B.A & DELL'ORSO, H. 2016 Identification and mitigation of TS waves using localized dynamic surface modification. *Phys. Fluids* **28** (6), 064103.

ANTONI, J. 2005 Blind separation of vibration components: principles and demonstrations. *Mech. Syst. Signal Process.* **19** (6), 1166–1180.

BOIKO, A.V., DOVGAL, A.V., GREK, G.R. & KOZLOV, V.V. 2011 *Physics of Transitional Shear Flows: Instability and Laminar–Turbulent Transition in Incompressible Near-Wall Shear Layers*, vol. 98. Springer.

BRUNTON, S.L., ROWLEY, C.W & WILLIAMS, D.R. 2013 Reduced-order unsteady aerodynamic models at low Reynolds numbers. *J. Fluid Mech.* **724**, 203–233.

CHERRY, E.C. 1953 Some experiments on the recognition of speech, with one and with two ears. *J. Acoust. Soc. Am.* **25** (5), 975–979.

CICHOCKI, A., ZDUNEK, R. & AMARI, S.-I. 2007 Hierarchical ALS algorithms for nonnegative matrix and 3D tensor factorization. *Lect. Notes Comput. Sci.* **4666**, 169–176.

CICHOCKI, A., ZDUNEK, R., PHAN, A.H. & AMARI, S.-I. 2009 *Nonnegative Matrix and Tensor Factorizations: Applications to Exploratory Multi-Way Data Analysis and Blind Source Separation*. John Wiley & Sons.

COHEN, J. 1994 The initial evolution of a wave packet in a laminar boundary layer. *Phys. Fluids* **6** (3), 1133–1143.

CORKE, T.C., POST, M.L. & ORLOV, D.M. 2009 Single dielectric barrier discharge plasma enhanced aerodynamics: physics, modeling and applications. *Exp. Fluids* **46** (1), 1–26.

FABBIANE, N., SIMON, B., FISCHER, F., GRUNDMANN, S., BAGHERI, S. & HENNINGSON, D.S. 2015 On the role of adaptivity for robust laminar flow control. *J. Fluid Mech.* **767**, R1.

FRANSSON, J.H.M. 2004 Leading edge design process using a commercial flow solver. *Exp. Fluids* **37** (6), 929–932.

GAO, B., LU, P., WOO, W.L., TIAN, G.Y., ZHU, Y. & JOHNSTON, M. 2018 Variational Bayesian subgroup adaptive sparse component extraction for diagnostic imaging system. *IEEE Trans. Ind. Electron.* **65** (10), 8142–8152.

GASTER, M. 1975 A theoretical model of a wave packet in the boundary layer on a flat plate. *Proc. R. Soc. Lond.* A **347** (1649), 271–289.

GASTER, M. & GRANT, I. 1975 An experimental investigation of the formation and development of a wave packet in a laminar boundary layer. *Proc. R. Soc. Lond.* A **347** (1649), 253–269.

GLUZMAN, I., OSHMAN, Y. & COHEN, J. 2020 Detection and isolation of Tollmien–Schlichting waves in shear flows using blind source separation. *Mech. Syst. Signal Process.* **136**, 106485.

GREENBLATT, D., GOEKSEL, B., RECHENBERG, I., SCHÜLE, C.Y., ROMANN, D. & PASCHEREIT, C.O. 2008 Dielectric barrier discharge flow control at very low flight Reynolds numbers. *AIAA J.* **46** (6), 1528–1541.

HAYKIN, S. & CHEN, Z. 2005 The cocktail party problem. *Neural Comput.* **17** (9), 1875–1902.

HYVÄRINEN, A. & OJA, E. 2000 Independent component analysis: algorithms and applications. *Neural Netw.* **13** (4), 411–430.

JORDINSON, R 1970 The flat plate boundary layer. Part 1. Numerical integration of the Orr–Sommerfeld equation. *J. Fluid Mech.* **43** (04), 801–811.

KIM, J. & BEWLEY, T.R. 2007 A linear systems approach to flow control. *Annu. Rev. Fluid Mech.* **39**, 383–417.

KIM, K.J., JANG, C.S., JEONG, J.-M. & NAM, S.W. 2006 Acoustic echo cancellation using the duet algorithm based blind separation in a noisy environment. In *TENCON 2006 - 2006 IEEE Region 10 Conference*, pp. 1–4. IEEE.

KRIEGSEIS, J., SIMON, B. & GRUNDMANN, S. 2016 Towards in-flight applications? A review on dielectric barrier discharge-based boundary-layer control. *Appl. Mech. Rev.* **68** (2), 020802.

LI, Y. & GASTER, M. 2006 Active control of boundary-layer instabilities. *J. Fluid Mech.* **550**, 185–205.

MOREAU, E. 2007 Airflow control by non-thermal plasma actuators. *J. Phys.* D*: Appl. Phys.* **40** (3), 605.

NOGUEIRA, L.C.F. & PETRAGLIA, M.R. 2015 Robust localization of multiple sound sources based on BSS algorithms. In *2015 IEEE 24th International Symposium on Industrial Electronics (ISIE)*, pp. 579–583. IEEE.

OPFER, H., EVERT, F., RONNEBERGER, D. & GROSCHE, F.R. 2004 On the potential and the limitations of boundary-layer stabilization via active wave cancellation. In *Recent Results in Laminar-Turbulent Transition* (ed. S. Wagner, M. Kloker, U. Rist), Notes on Numerical Fluid Mechanics and Multidisciplinary Design, vol. 86. pp. 219–230. Springer.

OSHMAN, Y. & MARKLEY, F.L. 1999 Spacecraft attitude/rate estimation using vector-aided GPS observations. *IEEE T. Aero. Elec. Sys.* **35** (3), 1019–1032.

OZEROV, A & FEVOTTE, C. 2010 Multichannel nonnegative matrix factorization in convolutive mixtures for audio source separation. *IEEE Trans. Audio Speech* **18** (3), 550–563.

PEDERSEN, M.S., LARSEN, J., KJEMS, U. & PARRA, L.C. 2007 A survey of convolutive blind source separation methods. In *Multichannel Speech Processing Handbook* (ed. J. Benesty, Y. Huang, M. Sondhi), pp. 1065–1084. Springer.

RICKARD, S. 2007 The DUET blind source separation algorithm. In *Blind Speech Separation* (ed. S. Makino, H. Sawada, T.W. Lee), pp. 217–241. Springer.

ROWLEY, C.W. 2005 Model reduction for fluids, using balanced proper orthogonal decomposition. *Intl J. Bifurcation Chaos* **15** (03), 997–1013.

SARIC, W.S. 2008 Experiments in 2-D boundary-layers: stability and receptivity advances in laminar-turbulent transition modelling, NATO educational notes.

SAWADA, H., ARAKI, S. & MAKINO, S. 2010 Underdetermined convolutive blind source separation via frequency bin-wise clustering and permutation alignment. *IEEE Trans. Audio Speech* **19** (3), 516–527.

SCHMID, P.J. 2010 Dynamic mode decomposition of numerical and experimental data. *J. Fluid Mech.* **656**, 5–28.

SCHMID, P.J. & HENNINGSON, D.S. 2001 Stability and transition in shear flows, vol. 142. Springer Science & Business Media.

SEMERARO, O., BAGHERI, S., BRANDT, L. & HENNINGSON, D.S. 2013 Transition delay in a boundary layer flow using active control. *J. Fluid Mech.* **731**, 288–311.

SERVIERE, C. & FABRY, P. 2005 Principal component analysis and blind source separation of modulated sources for electro-mechanical systems diagnostic. *Mech. Syst. Signal Process.* **19** (6), 1293–1311.

SILVA, M., FIGUEIREDO, E., COSTA, J.C.W.A. & MASCARE NAS, D. 2020 Spatio-temporal decomposition of 2d travelling waves from video measurements. *Mech. Syst. Signal Process.* **139**, 106599.

SIPP, D. & SCHMID, P.J. 2016 Linear closed-loop control of fluid instabilities and noise-induced perturbations: a review of approaches and tools. *Appl. Mech. Rev.* **68** (2), 020801.

STURZEBECHER, D. & NITSCHE, W. 2003 Active cancellation of Tollmien–Schlichting instabilities on a wing using multi-channel sensor actuator systems. *Intl J. Heat Fluid Flow* **24** (4), 572–583.

TAIRA, K., BRUNTON, S.L, DAWSON, S.T.M., ROWLEY, C.W., COLONIUS, T., MCKEON, B.J., SCHMIDT, O.T, GORDEYEV, S., THEOFILIS, V. & UKEILEY, L.S. 2017 Modal analysis of fluid flows: an overview. *AIAA J.* **55** (12), 4013–4041.

TAYLOR, J.A. & GLAUSER, M.N. 2004 Towards practical flow sensing and control via pod and lse based low-dimensional tools. *Trans. ASME J. Fluids Engng* **126** (3), 337–345.

TREFETHEN, L.N. 2000 *Spectral Methods in MATLAB*, vol. 10. SIAM.

VADAREVU, S.B., SYMON, S., ILLINGWORTH, S.J. & MARUSIC, I. 2019 Coherent structures in the linearized impulse response of turbulent channel flow. *J. Fluid Mech.* **863**, 1190–1203.

VIGARIO, R. & OJA, E. 2008 BSS and ICA in neuroinformatics: from current practices to open challenges. *IEEE Rev. Biomed. Engng* **1**, 50–61.

WANG, Y., YILMAZ, Ö. & ZHOU, Z. 2013 Phase aliasing correction for robust blind source separation using duet. *Appl. Comput. Harmon. Anal.* **35** (2), 341–349.

YILMAZ, O. & RICKARD, S. 2004 Blind separation of speech mixtures via time-frequency masking. *IEEE Trans. Signal Process.* **52** (7), 1830–1847.

YOSHIOKA, T., NAKATANI, T., MIYOSHI, M. & OKUNO, H.G. 2010 Blind separation and dereverberation of speech mixtures by joint optimization. *IEEE Trans. Audio Speech* **19** (1), 69–84.

ZHANG, J., GAO, H., LIU, Q., FARZADPOUR, F., GREBE, C. & TIAN, Y. 2017 Adaptive parameter blind source separation technique for wheel condition monitoring. *Mech. Syst. Signal Process.* **90**, 208–221.

ZHEN, L., PENG, D., YI, Z., , XIANG, Y. & CHEN, P. 2017 Underdetermined blind source separation using sparse coding. *IEEE Trans. Neural Netw. Learn. Syst.* **28** (12), 3102–3108.